Journal of Nanobiotechnology

RESEARCH Open Access

Three-dimensional bioprinting of patient-derived Gastrointestinal stromal tumor: a novel platform for precision oncology and drug response profiling

Liwei Du[1†], Zicheng Zheng[2†], Yanan Wang[3†], Kai Zhang[1], Yuce Lu[1], Minghao Sun[1], Mingchang Pang[1], Shangze Jiang[1], Yixuan He[2], Shunda Du[1], Haitao Zhao[1], Yilei Mao[1*], Huayu Yang[1*] and Weiming Kang[2*]

Abstract

Background Gastrointestinal stromal tumors (GISTs) exhibit significant heterogeneity, posing substantial challenges for personalized treatment strategies. Patients often display varied responses to different therapeutic agents and dosages. Currently, the absence of robust and physiologically relevant in vitro models for GISTs impedes accurate prediction of therapeutic efficacy, thereby constraining the advancement of effective treatment strategies. Traditional 2D cell cultures fail to replicate the tumor microenvironment (TME) and lack patient-specific characteristics, limiting their predictive value. In contrast, three-dimensional bioprinting (3DP) technology faithfully recapitulates key histological architecture and molecular features of their parental tumors, enhancing the physiological relevance of in vitro models.

Methods We employed patient-derived 3DP-GIST models via 3D bioprinting technology, followed by comprehensive histopathological, genomic, and transcriptomic analyses. Subsequently, we applied clinically approved targeted therapeutic agents to perform drug screening and response prediction on the 3DP-GIST models. The drug sensitivity profiles obtained from these models were then correlated with retrospective clinical data and patient follow-up records to assess the models' potential in guiding the selection and prediction of effective GIST therapies.

Results In our study, we successfully constructed 12 patient-derived 3DP-GIST models. Histopathological assessments, whole-exome sequencing (WES), and transcriptomic analyses confirmed that these models accurately

†Liwei Du, Zicheng Zheng and Yanan Wang contributed equally to this work.

*Correspondence:
Yilei Mao
pumch-liver@hotmail.com
Huayu Yang
dolphinyahy@hotmail.com
Weiming Kang
Kangwm@pumch.cn

Full list of author information is available at the end of the article

recapitulate the histological architecture, biomarker expression, and molecular features of their corresponding parental tumors. Transcriptomic profiling further revealed gene expression signatures associated with GIST recurrence risk and imatinib resistance. Importantly, the 3DP-GIST models demonstrated the capacity to provide precise, individualized treatment recommendations within 10 days post-surgery, potentially reducing treatment delays and improving patient outcomes.

Conclusions Overall, the 3DP-GIST model represents a robust and efficient platform for evaluating patient-specific drug sensitivities in vitro, thereby guiding personalized therapeutic strategies for GIST patients.

Keywords Gastrointestinal stromal tumor, Three-dimensional bioprinting, Drug screening, Personalized medicine, Precision oncology

Introduction

Gastrointestinal stromal tumors (GISTs), the most prevalent mesenchymal neoplasms of the digestive tract, predominantly arise from interstitial cells of Cajal in the stomach (60–70%) or small intestine (20–30%) [1, 2]. Oncogenic driver mutations in KIT (75–80%) or PDGFRA (5–10%) receptor tyrosine kinases not only initiate tumorigenesis but critically determine therapeutic responses [3]. The disease exhibits profound heterogeneity, ranging from indolent lesions maintaining stability for decades, to aggressive subtypes demonstrating rapid metastatic progression [4]. Despite remarkable initial responses to the tyrosine kinase inhibitor imatinib, intrinsic and acquired resistance limits long-term efficacy. However, approximately 10–15% of patients display primary resistance to imatinib, and nearly 50% develop secondary resistance within two years of therapy [5]. In advanced settings, the evolution of drug-resistant mutations is unstoppable, leading to poor prognosis for patients. Sunitinib, regorafenib, and ripretinib serve as second- and third-line agents, but median progression-free survival (mPFS) remains limited to about six months [6–8].

High-throughput next generation sequencing (NGS) has enabled comprehensive mapping of GIST mutational landscapes, informing prognostic stratification and therapeutic decisions [9–12]. Nevertheless, the presence of a targetable mutation does not guarantee clinical response, as additional genetic, epigenetic, and microenvironmental factors modulate drug sensitivity. Therefore, the integration of NGS-guided genomic profiling with functional drug sensitivity testing represents a paradigm shift in GIST management, which can more accurately predict individual responses, shorten the therapeutic window, and ultimately improve patient outcomes.

However, the absence of dedicated GIST-specific public repositories and representative in vitro cellular models has markedly hindered the identification and preclinical validation of new therapeutic targets and treatment strategies. Consequently, it is imperative to develop robust ex vivo drug-screening platforms that faithfully recapitulate the individual characteristics of GIST patients. To date, only a handful of GIST cell lines have been successfully established, due to the absence of the extracellular matrix (ECM) capable of maintaining tissue homeostasis and modulating tumor behavior, which cannot reproduce the complex functional interactions within the tumor microenvironment, rendering them inadequate for guiding personalized treatment strategies [13, 14].

Recent advancements in 3D bioprinting (3DP) have revolutionized precision oncology by enabling the construction of patient-derived tumor models that address critical preclinical challenges [15]. Numerous investigations have shown that 3DP models provide a robust, high-throughput, and economically viable platform for drug screening. The integration of programmable, computer-aided automation further standardizes the bioprinting workflow, enabling high-throughput and reproducible model generation. By combining patient-derived tumor cells with hydrogels possessing excellent mechanical strength and biocompatibility, 3D bioprinting can rapidly recreate the morphological and biological features of the original tumor. Leveraging these advantages, a variety of solid-tumor 3DP models, including glioma, lung, pancreatic, liver, and colorectal cancers, which have been established to faithfully recapitulate the drug response profiles of their parental tumors [16–20]. However, reports of 3D culture models for GIST remain scarce, and 3DP technology is ideally suited to fill this gap.

In this study, we leveraged extrusion-based 3D bioprinting with a gelatin methacryloyl (GelMA)/hyaluronic acid methacryloyl (HAMA) composite hydrogel to construct, characterize, and perform drug sensitivity testing on 12 patient-derived 3DP-GIST models. These models faithfully recapitulated the histopathological architecture and molecular heterogeneity of their parental tumors, enabling identification of marker genes associated with sensitivity or resistance to targeted agents. We further demonstrated the utility of 3DP-GISTs as high-throughput, preclinical platforms for drug prediction and screening, providing a robust foundation for advancing personalized therapeutic strategies in GIST.

Materials and methods

Patient-derived specimens for 3D Bioprinting

All experiments involving tissue collection underwent rigorous evaluation and received approval from the Ethics Review Committee at Peking Union Medical College Hospital (Approval No. I-25PJ0659). GIST tissues were procured from patients who underwent laparoscopic gastrectomy in the General Surgery Department of the same institution. Postoperative clinical data for GIST patients were extracted from the hospital's medical records database, including radiological information from computed tomography (CT) scans and subsequent follow-up details.

Bioprinting construction and culture of 3DP-GISTs

Fresh GIST tumor specimens were obtained from surgical resections with patient consent and institutional ethics approval. Samples were immediately transported on ice in sterile sample preservation solution: Advanced DMEM/F12 medium supplemented with 0.2% primocin, 1% antibiotic-antimycotic, and 10 μM ROCK inhibitor Y-27,632, and delivered to the laboratory within four hours for subsequent experimental procedures. After removal of necrotic areas and blood clots, viable tumor regions were minced into ~1 mm^3 fragments, subsequently incubated in 10 mL of a digestion medium composed of 1.0 mg/mL collagenase I (Gibco), 1.5 mg/mL collagenase IV (Gibco), 20 μg/mL hyaluronidase (Sigma-Aldrich), 1 mg/mL dispase type II (Sigma-Aldrich), 10 μM Y-27,632, 1% antibiotic-antimycotic, and 0.2% primocin (Invivogen). The incubation was conducted on an orbital shaker at 37 °C for 30 to 60 min. A cell suspension was prepared by repeatedly dissociating the digested tissue using a 1000 μL pipette (Corning), followed by filtration through a 100 μm cell strainer. The cell suspension was then centrifuged at 300 g for five minutes at 4 °C. If the pellet contained significant red blood cells, 1 mL of Advanced DMEM/F12 and 3 mL of Red Blood Cell lysis buffer (Servicebio) were added at 4 °C for 10 min, followed by centrifugation at 300 g for five minutes at 4 °C. To thoroughly remove impurities, the cell pellet was washed with 5 mL of advanced DMEM/F12 and centrifuged again at 300 g for five minutes at 4 °C. Finally, the cell pellet was resuspended in human 3DP-GIST culture medium following cell counting, preparing it for 3D bioprinting.

Our investigation assessed various biomaterial compositions to develop a biocompatible hydrogel system for GIST cells. The bioink, used in all bioprinting procedures, was formulated by amalgamating 7% gelatin methacryloyl (GelMA) and 0.1% hyaluronic acid methacryloyl (HAMA) supplemented with the photoinitiator lithium phenyl-2,4,6-trimethylbenzoylphosphinate (LAP), which were homogenized and stored at 37 °C in darkness before printing. To ensure maximal cell viability, the cell suspension was mixed with the bioink at a 1:1 ratio immediately prior to printing, resulting in a final cell density of 5×10^6 cells mL^{-1}. The bioink-cell-biomaterial mixture was then loaded into a 3 mL syringe fitted with a 23 G needle. After incubating for 10 min at 4 °C to promote gel formation, the syringe was loaded onto a light-cured 3D bioprinter (SUNP Biotech). The 3D-BP constructs were designed using BioMaker 2i software (SUNP Biotech). To preserve structural fidelity during bioprinting, thermal conditions for the extrusion nozzle and chamber were precisely maintained at 20.5 °C and 14.5 °C, respectively. The 3DP-GIST model featured a stratified grid configuration with dimensions of 6 mm × 6 mm × 0.8 mm, along with a layer height of 0.2 mm and a line width of 1.0 mm. Printing parameters were set with an extrusion rate of 1 mm^3 s^{-1} and a printing speed of 6 mm^3 s^{-1}. The entire printing process was completed within 2 h, with the 3DP-GIST structures fabricated onto 48-well plates on the chamber platform. Post-bioprinting, the constructs were subjected to 405 nm light exposure at an intensity of 15 mW/cm^2 for 20 s to initiate GelMA and HAMA crosslinking. The constructs were subsequently rinsed with HBSS and cultured in human 3DP-GIST culture medium at 37 °C with 5% CO_2. All bioprinting and culture steps were conducted under aseptic conditions in a biosafety cabinet. The culture medium contained 1% penicillin-streptomycin and 0.2% Primocin to prevent bacterial or fungal growth. During the entire culture period, sterility was evaluated by daily microscopic inspection. Contaminated cultures were discarded.

We modified the 3DP-GIST culture medium based on previous reports [21–23], which contained advanced DMEM/F12 (Gibco), 1× B27 supplement (Life Technologies), 1× N2 supplement (Life Technologies), 2 mM GlutaMAX (Gibco), 10 mM HEPES (Gibco), 50 ng mL^{-1} recombinant EGF (PeproTech), 200 ng mL^{-1} Recombinant Human FGF-10 (PeproTech), 100 ng mL^{-1} Recombinant Human Noggin (PeproTech), 100 ng mL^{-1} Recombinant Human Wnt3a V3 (Novoprotein), 500 ng mL^{-1} Recombinant Human R-Spondin1 (Novoprotein), 1.25 mM N-acetyl-L-cysteine (Sigma-Aldrich), 10 mM Nicotinamide (Sigma-Aldrich), 2 μM A8301 (Tocris Bioscience), 10 nM Gastrin I (Sigma-Aldrich), 30 ng mL^{-1} SCF (PeproTech), 100 ng mL^{-1} IGF-1 (PeproTech), 10 μM Forskolin (Sigma-Aldrich), 700 nM CHIR99021 (Sigma-Aldrich), 1% penicillin/streptomycin, and 10 μM Y27632. The culture medium was replaced every 3 days.

Rheology and mechanical behavior of Bioinks

The storage modulus (G′) and loss modulus (G″) of the bioink under different shear strains were measured using a rheometer (MCR 302; Anton Paar), while viscosity under varying shear stresses was characterized via a

precision universal tester (AGS-X-50 N; Shimadzu). Bioink samples were prepared in a light-protected environment to prevent premature crosslinking and carefully loaded onto the testing plates. All measurements were performed in triplicate to ensure data reproducibility and reliability.

Cryo-SEM analysis

For the Cryo-SEM analysis, the 3DP-GIST models were fixed with 2.5% glutaraldehyde and then snap-frozen in liquid nitrogen for 30 s. The unloaded cell hydrogel was snap-frozen directly. Samples were kept at low temperature and under vacuum, then transferred to a preparation chamber, sublimated at −90 °C, and sputter-plated with gold. Samples were imaged with an electron microscope (FEI Quanta 450) at −140 °C.

Cell survival analysis

Cell viability within the 3DP-GIST models was assessed using Calcein-AM (C-AM; Sigma-Aldrich) and propidium iodide (PI; Sigma-Aldrich) on days 1, 4, 7, 10, and 14 post-printing. Models were incubated with CAM/PI at 37 °C for 30 min in the dark, rinsed three times with PBS, and imaged using a laser-scanning confocal microscope (Nikon A1R, Tokyo, Japan). Viable and dead cells were quantified across five random fields using ImageJ software (version 1.53c, NIH, Bethesda, MD, USA). The cell survival rate was calculated as: (number of viable cells/total cells) × 100%.

H&E and immunohistochemistry (IHC) staining

Fresh GIST specimens and 3DP-GIST models were fixed with 4% paraformaldehyde (PFA) (Sigma-Aldrich) after culturing for 10 days. Upon completion of fixation, the tissues and 3DP models were embedded in paraffin, sectioned into 5-μm-thick segments, and subjected to H&E staining following standard protocols.

Paraffin-embedded tissue sections underwent deparaffinization and hydration using xylene and absolute ethanol prior to immunohistological staining. They were then treated with EDTA antigen retrieval solution (pH 8.0) to facilitate antigen retrieval. To block endogenous peroxidase activity, the slices were incubated in 3% hydrogen peroxide at room temperature for 15 min. Then slices were covered with 3% BSA at room temperature for half an hour. DOG-1 (Beyotime, AG8369, 1:200), CD117/c-Kit (Beyotime, AG8369, 1:200), and CD34 (Immunoway, PT0716R, 1:400) and were added and incubated overnight at 4 ℃. The slices underwent incubation with an HRP-conjugated goat anti-rabbit IgG secondary antibody (Servicebio, 1:200) at ambient temperature for a period of 50 min. The stained cells and sections were examined under a laser-scanning confocal microscope (Nikon A1R, Tokyo, Japan).

Western blot (WB) analysis

Protein lysates were extracted from matched parental tumor tissues and 3DP-GIST models using RIPA buffer supplemented with protease and phosphatase inhibitors (Roche). Protein concentrations were determined using the BCA assay (Thermo Fisher). Equal amounts of protein were separated by SDS-PAGE and transferred to PVDF membranes (Millipore). Membranes were blocked with 5% non-fat milk or BSA in TBS containing 0.1% Tween 20 (TBST) for 1 h at room temperature, followed by incubation overnight at 4 °C with primary antibodies: anti-KIT (1:1000, Cell Signaling Technology, 3074), anti-phospho-KIT (Tyr719) (1:1000, Cell Signaling Technology, 3391), anti-AKT (1:1000, Abclonal, A18675), anti-phospho-AKT (Ser473) (1:2000, Cell Signaling Technology, 4060 T), anti-ERK1/2 (1:1000, Abclonal, A4782), and anti-phospho-ERK1/2 (1:1000, Abclonal, AP0974). GAPDH (1:50000, Abclonal, A19056) was used as a loading control. After washing, membranes were incubated with HRP-conjugated secondary antibodies (Abclonal) for 1 h at room temperature. Signals were detected using an enhanced chemiluminescence (ECL) substrate (Thermo Fisher Scientific) and imaged with a ChemiDoc MP imaging system (Bio-Rad).

Whole-exome sequencing and mutation analysis

DNA from GIST tissues and 3DP-GIST models was extracted using DNeasy Blood & Tissue Kit (QIAGEN) following the manufacturer's protocol after culturing for 10 days. DNA quantity and purity were assessed using Qubit fluorometry and NanoDrop spectrophotometry, and DNA integrity was evaluated on a 1% agarose gel. Then the DNA which was fragmented by using Covaris M220 Focused-ultrasonicator (Covaris) were subjected to sequencing library construction. Exome capture was performed using the Agilent SureSelect Human All Exon V6 platform (Agilent, Santa Clara, CA, USA) and the final libraries were sequenced for paired-end 150 bp using the Illumina NovaSeq 6000 Sequencing System (Illumina, San Diego, CA, USA). The mean on-target coverage was 150× for tumor samples and 100× for 3DP models.

Sequence data were aligned to the human reference genome (GRCh37/HG19) using the Burrows-Wheeler Aligner (BWA, version 0.7.9a). Local realignment, base quality score recalibration, and duplicate read removal were performed using the Genome Analysis Toolkit (GATK) and Picard. SNVs and indels were simultaneously detected using the HaplotypeCaller function of GATK (v3.3.0). Copy number variations were detected by FACETS [24]. Mutation files were converted to MAF format using vcf2maf (version 1.6.21) and visualized using the R package maftools.

RNA-seq analysis

RNA from GIST tissue and 3DP-GIST models was extracted using TRIzol (Thermo Fisher) using standard procedure. The total RNA quantity and purity were evaluated with the Bioanalyzer 2100 and RNA 6000 Nano LabChip Kit (Agilent, CA, USA). High-quality RNA samples, characterized by an RIN number above 7.0, were utilized for sequencing library construction. Utilizing oligo(dT) (Thermo Fisher, USA) magnetic beads, mRNA was isolated and fragmented from total RNA in a precise procedure. Single-stranded cDNA was synthesized via reverse transcription of fragmented mRNA using random hexamer primers. Subsequently, this single-stranded cDNA was employed as a template for the synthesis of the complementary strand, resulting in the production of double-stranded cDNA. The cDNA libraries were subjected to end repair, A-tailing, and adapter ligation, followed by PCR amplification. The NEBNext Ultra™ RNA Library Prep Kit for Illumina (NEB, USA) was used to perform sequencing using a paired-end approach (2 * 150 bp) according to standard protocol.

The gene expression levels of each sample were quantified using RSEM v1.3.1. To achieve normalization across samples, FPKM, TPM and Count values were computed. Using the DESeq2 R package (1.46.0), differential expression analysis was performed based on the read counts obtained from gene expression level analysis [25]. The resulting P values were adjusted. The genes with the parameter of P value < 0.05 and absolute $\log_2$ fold change ≥ 1 were considered differentially expressed genes. Differentially expressed genes were then subjected to enrichment analysis of GO functions and KEGG pathways.

Transcriptomic concordance between 3DP-GIST models and matched primary tumor tissues was evaluated using Spearman's correlation coefficient (ρ) and the coefficient of determination (R^2) based on $\log_2$-transformed FPKM values. Spearman correlation coefficient (ρ) was calculated by "cor" function with parameter "method = spearman" in R package stats (v4.2.0) (www.r-project.org) and R square (R^2) was computed by "lm" function in R package stats v4.3.2 (www.r-project.org).

To assess the cellular composition and microenvironmental resemblance between 3DP-GIST models and parental tumors, we performed cell type deconvolution analysis using the xCell algorithm [26]. Bulk RNA-seq values from both 3DP-GIST models and matched primary tumors served as input for the analysis. xCell scores, reflecting the enrichment of 64 immune and stromal cell types, were calculated for each sample. To evaluate the concordance, we conducted a Pearson correlation analysis on the xCell enrichment scores from paired 3DP-GIST models and parental tumor tissues. Results were visualized through heatmaps, stacked bar plots, and scatter plots.

3DP-GIST drug testing

Drug testing was initiated on day 6 post-printing, followed by drug response assessment in the 3DP-GIST models. After a 6-day culture duration of the 3DP-GIST models, the cells were exposed to culture medium containing diverse concentrations of the drugs for a period of 72 h. The drugs included Imatinib (Selleck), Ripretinib (Selleck), Regorafenib (Selleck) and Sunitinib (Selleck). The concentration gradients used were as follows: Imatinib (0, 0.01, 0.1, 1, 10, 100 μM), Ripretinib (0, 0.01, 0.1, 1, 10, 50 μM), Regorafenib (0, 0.01, 0.1, 1, 10, 100 μM), Sunitinib (0, 0.01, 0.1, 1, 10, 100 μM). Cell viability was quantified at the 72-hour post-treatment time point through the CellTiter Glo 3D assay (Promega) according to the manufacturer's instructions. Dose-response curves were generated, and the log (IC50) and AUC values were computed using GraphPad Prism 10.0 (GraphPad Inc., La Jolla, CA, USA).

Correlation analysis between 3DP-GIST models and actual clinical outcomes

In accordance with the guidelines for GIST, patients were administered standard therapies following multidisciplinary consultations. In eligible surgical candidates, some were recommended to receive neoadjuvant therapy preceding surgery, while others underwent surgical intervention without prior neoadjuvant therapy. The Response Evaluation Criteria in Solid Tumors (RECIST) version 1.1 and Choi standard were used to evaluate the clinical response of patients after receiving drug treatment in this study, all tumor drug response of patients by three independent radiologists, respectively [27–29]. Drug responses of GIST patients were classified as PR (Partial Response), SD (Stable Disease), or PD (Progressive Disease) in this study. Tumor and node staging for all resected specimens were conducted according to the 7th American Joint Committee on Cancer TNM staging manual.

Statistical analysis

The clinical management of GIST patients utilized a classification system where individuals demonstrating PR or SD to drug treatment were categorized as sensitive to treatment (Response). In contrast, patients experiencing PD were classified as chemotherapy-resistant (Resistance). AUC was derived using Simpson's rule. Subsequently, the corresponding AUC value for each concentration interval was divided by its maximum value to obtain the normalized AUC. To investigate the correlation between in vitro chemosensitivity testing results and clinical outcomes in patients, normalized AUC values derived from 3DP-AUC models underwent ordering and were grouped into clusters via the Jenks Natural Breaks optimization algorithm [30]. The minimum number of

breaks required to attain a goodness-of-fit threshold exceeding 90% was established. By minimizing intragroup variance and maximizing intergroup variance, this algorithm determined cutoff values to differentiate between drug sensitivity and resistance in this study [31]. Correlative analysis between in vitro drug testing and clinical responses was implemented using the "jenks" function from the R package "classInt". The analyses were performed with R software v4.3.2 (www.r-project.org).

GraphPad Prism 10 (GraphPad Software Inc, San Diego, CA) was used for all statistical analyses and data visualization. All statistical analyses and data visualizations were performed using GraphPad Prism 10, with data presented as mean ± standard deviation. Statistical significance was defined as a p-value < 0.05, classified as follows: * $p < 0.05$; ** $p < 0.01$; *** $p < 0.001$; and ns for non-significant.

Results

Patient sample and clinical data

To establish personalized therapeutic platforms, we developed patient-derived 3DP-GIST models through systematic processing of surgically resected tumor specimens. Fresh tissue samples were dissociated via combined mechanical mincing and enzymatic digestion, isolated cells were encapsulated within tumor-specific bioink formulations and printed using optimized parameters [18, 32, 33]. Constructs were maintained in GIST-selective medium under physiological conditions, with histological validation and molecular profiling to ensure genomic-transcriptomic fidelity (Fig. 1A). This study enrolled 17 consecutive GIST patients who underwent curative resection at the Peking Union Medical College Hospital. All cases were histologically confirmed with risk stratification performed according to the modified NIH criteria: high-risk (n = 6, 50.0%), intermediate-risk (n = 5, 41.7%), low-risk (n = 1, 8.3%) [34]. The treatment cohort comprised 5 treatment-naïve patients (41.7%), 5 receiving neoadjuvant therapy (41.7%), and 2 with adjuvant therapy (16.7%). The most common neoadjuvant and postoperative treatments are imatinib, regorafenib, ripretinib, and sunitinib. Tumor localization was radiologically-pathologically correlated: 8 primary gastric tumors (predominantly in the body/antrum), and 4 small intestinal lesions (Fig. 1B, Supplementary Table S1).

Establishment of patient-derived 3DP-GIST models

We successfully established and maintained 12 three-dimensionally bioprinted GIST (3DP-GIST) models derived from patient tumor tissues, achieving a 70.6% success rate (12/17). Four cases failed due to insufficient tumor tissue (n = 3), low cellular viability (n = 1), or the pathological result was non-gastrointestinal stromal tumor (n = 1). Multi-omics profiling of the 12 validated models included whole-exome sequencing (WES) in 9 patients (75%), transcriptomic analysis in 7 (58.3%), and comprehensive drug sensitivity testing across all cases (n = 12, 100%). Building upon our prior research, we employed a GelMA/HAMA composite bioink system that demonstrated optimal rheological properties, biocompatibility, and print fidelity while effectively preserving tumor stemness [35–38]. This formulation synergistically integrates GelMA's tunable mechanical behavior with HAMA's tumor microenvironment-mimetic composition, addressing critical limitations of conventional matrigel-based systems. Therefore, in this study, we used this printing system to construct a 3DP-GIST model.

We developed an optimized primary tumor cell isolation protocol featuring sequential enzymatic digestion combined with mechanical dissociation through controlled pipetting. This novel approach significantly enhanced cellular yield and viability. The isolated cells were subsequently encapsulated within our GelMA/HAMA bioink and printed using a sterile, temperature-controlled extrusion-based high-precision bioprinter. To validate the excellent printability of the bioinks, we characterized their rheological properties. All formulations exhibited pronounced shear-thinning behavior, with viscosity decreasing by over three orders of magnitude as the shear rate increased from 0.1 to 100 s^{-1} (Fig. 1C). The representative stress-strain curves in Fig. 1D reveal that the incorporation of HAMA into the GelMA network markedly improved the hydrogel's elastic recovery. Strain amplitude sweeps showed a characteristic solid-to-liquid transition across all formulations, with loss modulus (G") exceeding storage modulus (G') as the strain increased from 1% to 25% (Fig. 1E). Visualization was performed using a scanning electron microscope, cell clusters, and the internal structure of the hydrogel. It shows that there is a rich and uniform pore network in the GelMA/HAMA composite hydrogel, in which the primary GIST is assembled into clusters of different sizes (Fig. 1F).

To systematically characterize 3DP-GIST models, we performed longitudinal bright-field imaging analysis. Longitudinal viability analysis via dual Calcein-AM (C-AM) and propidium iodide (PI) staining revealed sustained cell viability and progressive proliferation, with more than 85% of cells remaining viable in the 3DP models over a two-week period, thereby confirming robust microenvironmental support (Fig. 1G, H). In accordance with the findings of preceding studies, tumor cells self-assembled and aggregated into clusters in hydrogel scaffolds (Supplementary Fig. S1). However, there was significant heterogeneity of GIST cells from different patient sources, as evidenced by limited cell proliferation rates and assembly morphology [18, 20, 39, 40].

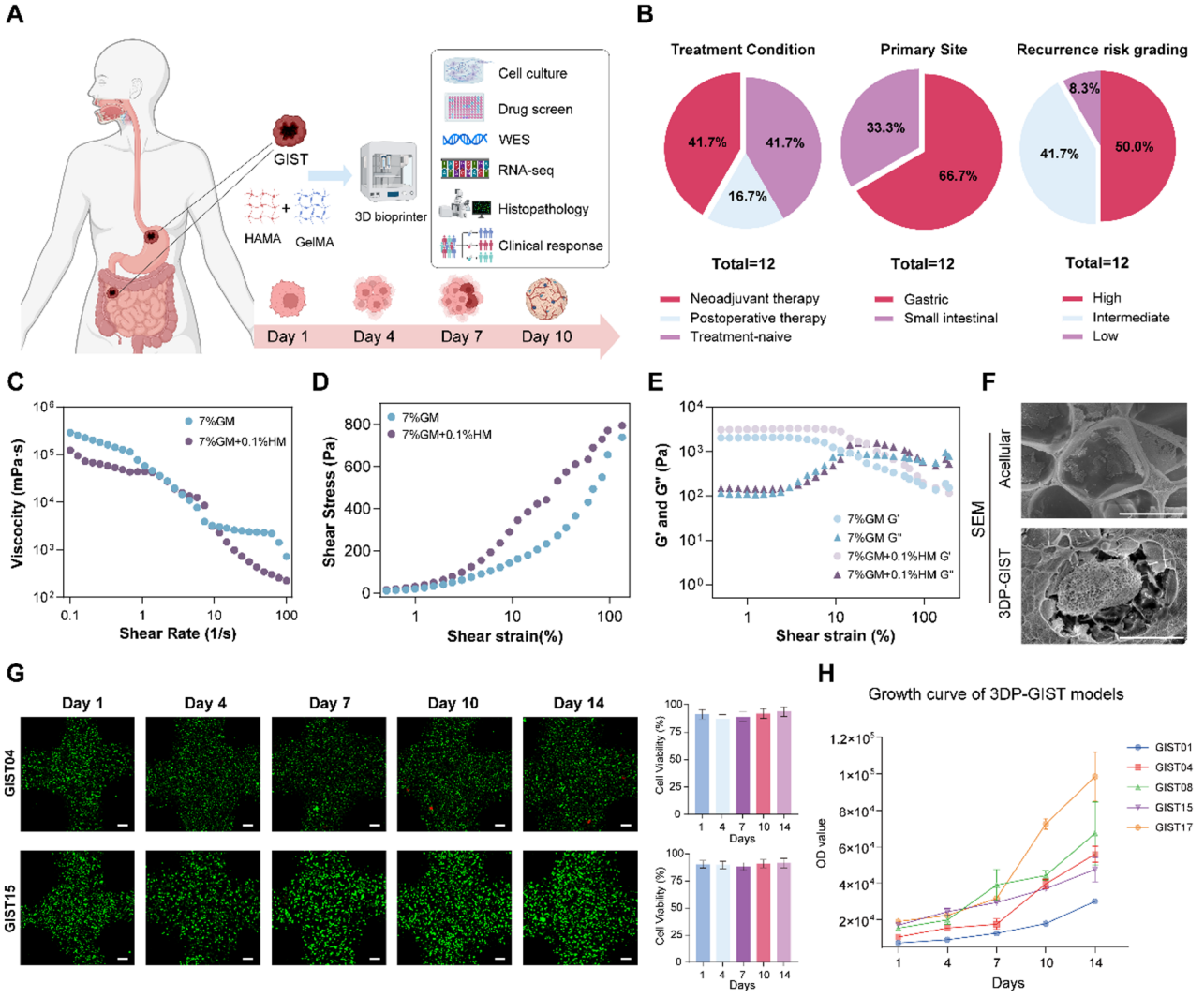

Fig. 1 Establishment of patient-derived 3DP-GIST models. **A.** Overview of process for constructing 3DP-GISTs, functional validation, and drug susceptibility testing. **B**. Pie charts showing treatment, tumor source, and recurrence risk grading for the 12 GIST patients. **C**. Viscosity and shear thinning behavior of different hydrogel systems at 37 °C. **D**. Representative compression curves of different hydrogel systems at 37 °C. **E**. Storage modulus (G′) and loss modulus (G″) of different hydrogel systems at 37 °C as a function of applied oscillatory strain. **F**. SEM images of cell clusters within a 3DP-GIST model (lower) and acellular GelMA/HAMA ECM (upper). Scale bar: 10 μm. **G**. Cell viability was assessed at day 1, 3, 7, 10, and 14 post-3DP, Live (green)/Dead (red). The relative cell survival rate was shown in the histogram. Scale bar: 100 μm. **H**. Representative growth curves for the 3DP-GIST model. OD values were obtained using the CellTiter-Glo 3D cell viability assay ($n = 3$, data expressed as means ± SD)

The patient-derived GIST cells maintained parental tumor characteristics within GelMA/HAMA scaffolds, preserving spindle-shaped and epithelioid morphotypes in the porous microenvironment of GelMA/HAMA bioink, and could gradually proliferate into diverse and irregular 3D self-assembled organ-like morphological structures after bioprinting, no association was found between cell morphology and risk of sample recurrence (Fig. 2A). GIST inherently exhibit multilevel heterogeneity, encompassing cellular morphology, histoarchitectural patterns, and molecular profiles [3, 41]. The 3DP-GIST model from different patients exhibited a diversity of growth rates and morphology, suggesting that tumor heterogeneity was maintained in patients. Histopathological evaluation demonstrated striking concordance between 3DP-GIST models and parental tumors, with Hematoxylin and eosin (H&E) staining revealing preserved subtype-specific architectures. Spindle-cell models (GIST02/05/08) recapitulated characteristic vacuolated pseudocystic structure, while the epithelioid model (GIST15) formed thin-walled luminal cysts mirroring clinical specimen. Furthermore, the 3DP-GIST model retains more subtle cytological features, including large, dark staining of nuclei, irregular arrangement, and reduced cytoplasmic ratio.

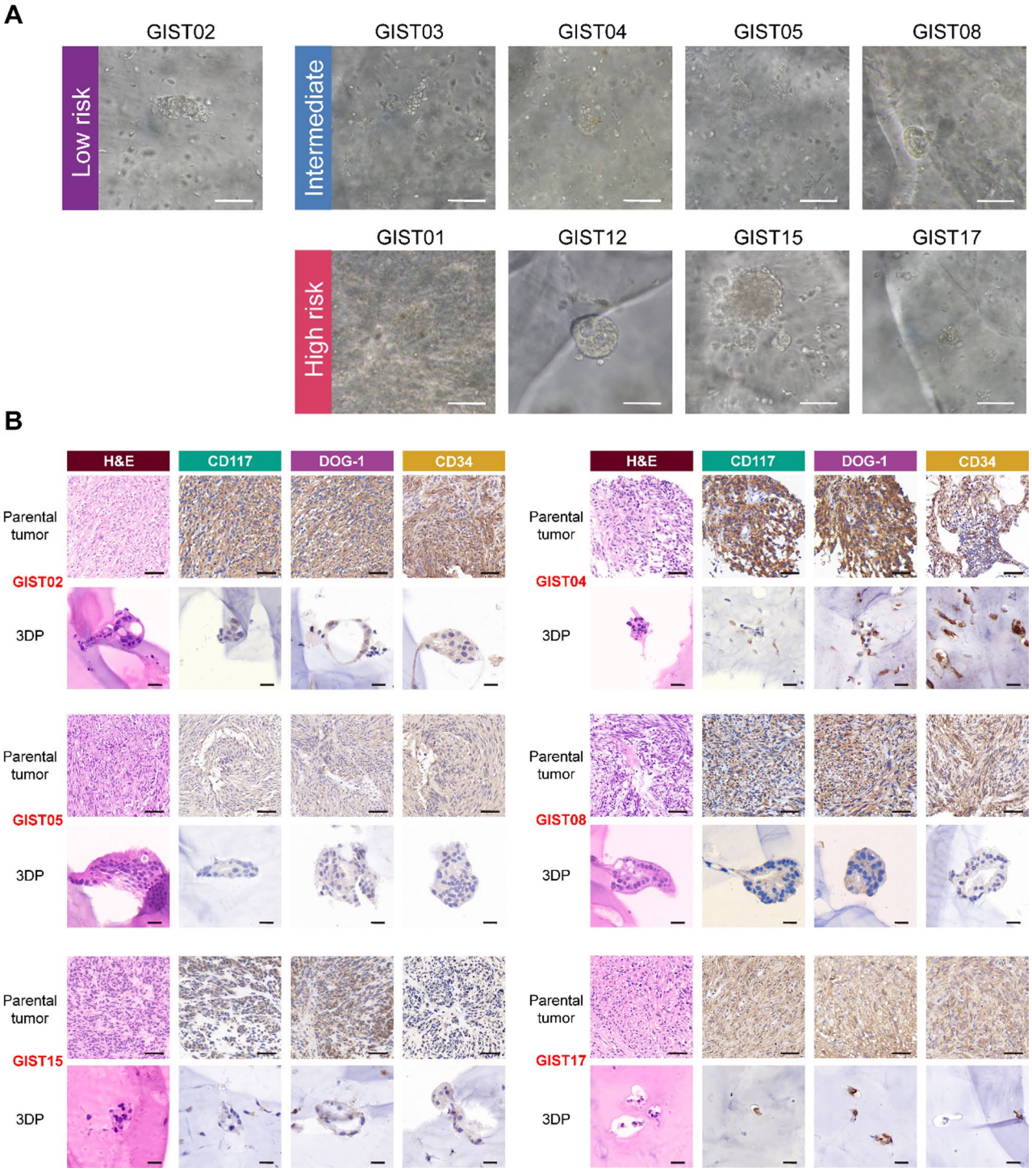

Fig. 2 3DP-GIST models recapitulate the morphological and histopathological features of matched patient tumors. **A.** Bright-field image of 3DP-GIST models derived from distinct recurrence risk patients in day 10 post-bioprinting. Scale bar: 100 μm. **B**. Hematoxylin and eosin (H&E) and immunohistochemical (IHC) staining for GIST markers CD117, DOG-1 and CD34 in 3DP-GISTs and corresponding parental tumors. Scale bar of tumors: 50 μm. Scale bar of 3DP-GISTs: 20 μm

Notably, the 3DP-GIST models demonstrated robust retention of parental tumor biomarker expression patterns, a critical validation of their clinical fidelity. Immunohistochemical profiling revealed preserved expression intensities and spatial distribution for diagnostic markers CD117, DOG-1 and CD34. Notably, patient GIST01 was diagnosed with wild-type GIST, and immunohistochemical (IHC) analysis of the primary tumor tissue revealed

negative DOG1 expression. This finding was consistently mirrored in the corresponding 3DP-GIST model, which also exhibited DOG1 negativity (Supplementary Fig. S2). Given that DOG1 is typically expressed in the majority of GISTs and serves as a sensitive and specific diagnostic marker, its absence in both the primary tumor and the 3DP-GIST model underscores the model's fidelity in recapitulating the unique molecular characteristics of the patient's tumor. These alignments further validate the utility of the 3DP-GIST model in accurately reflecting patient-specific tumor biology.

To further biochemically validate the functional integrity of oncogenic signaling pathways, particularly the crucial KIT downstream pathway, in our 3DP-GIST models, we performed Western blot analysis on protein lysates from matched parental tumor tissues (T) and 3DP-GIST models (P). We analyzed the expression and phosphorylation status of KIT, AKT, and ERK1/2, with GAPDH as a loading control. Supplementary Fig. S3 presents representative Western blot results for four distinct patients (GIST09, GIST10, GIST11, and GIST14). For each patient, we consistently observed strong expression of total KIT, AKT, and ERK1/2. More importantly, robust phosphorylation of KIT (p-KIT), AKT (p-AKT), and ERK1/2 (p-ERK1/2) was evident in both the original tumor tissues and their respective 3DP-GIST models. The patterns and levels of phosphorylation in the 3DP-GIST models closely mirrored those in the corresponding parental tumors. This direct biochemical evidence unequivocally confirmed that the critical KIT-driven oncogenic signaling cascades, which are fundamental to GIST pathogenesis and therapeutic response, are faithfully maintained ex vivo in our 3DP models. This functional fidelity further strengthens the utility and translational potential of our platform for studying GIST biology and drug response mechanisms.

The 3DP-GIST model retains the mutation profile of its corresponding parental tumor

In previous studies, our team demonstrated that patient-derived 3D-bioprinted (3DP) tumor models recapitulate the genomic mutation profiles of parental tumors. To systematically evaluate the concordance of somatic mutations and DNA copy number variations (CNVs) between 3DP-GIST models and their matched parental tumor samples, we performed whole-exome sequencing (WES) and comprehensive analysis. Results revealed that the single-nucleotide variants (SNV) and insertion/deletion (indel) ratios within each paired group further confirmed their mutual similarity (Fig. 3A). The most frequent somatic base substitution in both 3DP-GIST models and parental tumors was C > T/G > A transitions (Ti), while the least common mutation type was T > A/A > T transversions (Tv), consistent with previously described GIST mutational signatures (Supplementary Fig. S4) [41].

To investigate the preservation of tumor-specific mutational signatures in our 3DP-GIST models, we analyzed somatic variants identified by Alexandrov et al. and a compiled list of over 40 recurrently mutated genes from the COSMIC GIST cohort and recent GIST genome sequencing studies [41–45]. We fitted these somatic SNV profiles to both our primary tumor samples and their matched 3DP-GIST models, then quantified the retention of signature variants. Notably, each of the nine 3DP-GIST models retained approximately 85% of the common GIST-associated mutations observed in its parental tumor (Fig. 3B).

While the 3DP-GIST models largely recapitulate the genomic landscape of their source tumors, some distinctions remain (Fig. 3C). Notably, the 3DP-GIST models effectively preserved primary parental mutations, including *TMEM14B*, *PDE4DIP*, *BCLAF1*, and *NBPF10*. In addition, characteristic GIST-associated mutations such as *KIT*, *KMT2C*, *CACNA1A*, *RB1*, *SDHC*, and *ARID1B* were also detected in our samples [46]. The retention of these mutations underscores the fidelity of the 3DP-GIST models in maintaining the genetic heterogeneity of the original tumors. Notably, neither the primary tumors nor the corresponding 3DP models harbored tumor-specific mutations exceeding the expected threshold, consistent with the characteristically low mutational burden of GIST [41]. Elucidating these genome-level variations underlying tumor heterogeneity may shed light on GIST pathogenesis and mechanisms of targeted-therapy resistance, thereby informing the development of more effective treatment strategies. CNV analysis demonstrated that 3DP-GISTs and their matched parental tumors share highly similar patterns of genomic losses and gains (Fig. 3D).

We compared our somatic alteration landscape with that reported by Xie et al. [47] Although the types of driver alterations detected in our cohort are consistent with prior reports, the absolute frequency of KIT mutations is lower in our dataset. This discrepancy is likely due to cohort-specific factors, including the modest sample size, partial WES coverage of the cohort, inclusion of wild-type GIST cases, and possible differences in tumor purity or prior treatment history. Despite these differences, each 3DP-GIST model showed a high level of concordance with its parental tumor. These results demonstrate that the 3DP-GIST models preserve the core genomic architecture of their original tumors while reflecting the molecular diversity observed in GISTs.

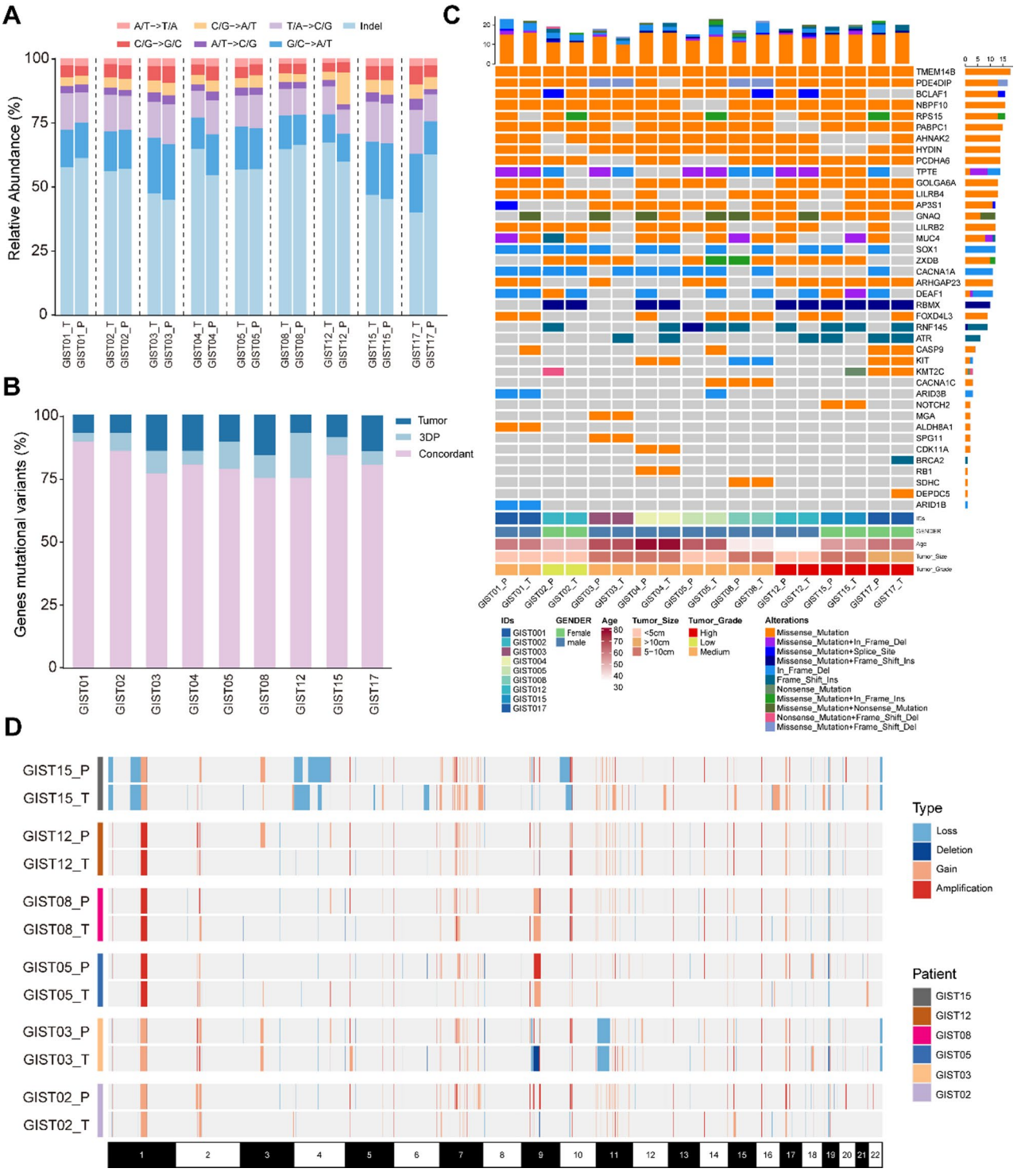

Fig. 3 3DP-GIST models recapitulated the main genetic features of parental tumors. **A.** Proportion of exon variants in 3DP-GISTs and matched parental tumors. **B**. Concordance of single-nucleotide variants (SNVs) screened in 3DP-GISTs and parental tumors. **C**. Overview of somatic mutations in the 3DP-GISTs and their parental tumors. **D**. Copy number variation (CNV) landscape between 3DP-GIST model and paired parental tumors

The 3DP-GIST model successfully recapitulates the transcriptomic characterization of parental tumors

To gain deeper insight into the transcriptomic landscape of the 3DP-GIST system, RNA sequencing (RNA-seq) was carried out on the 3DP-GIST models and their matched parental tumors. Pearson correlation analysis revealed a strong concordance between each matched 3DP-GIST model and its parental tumor, indicating that

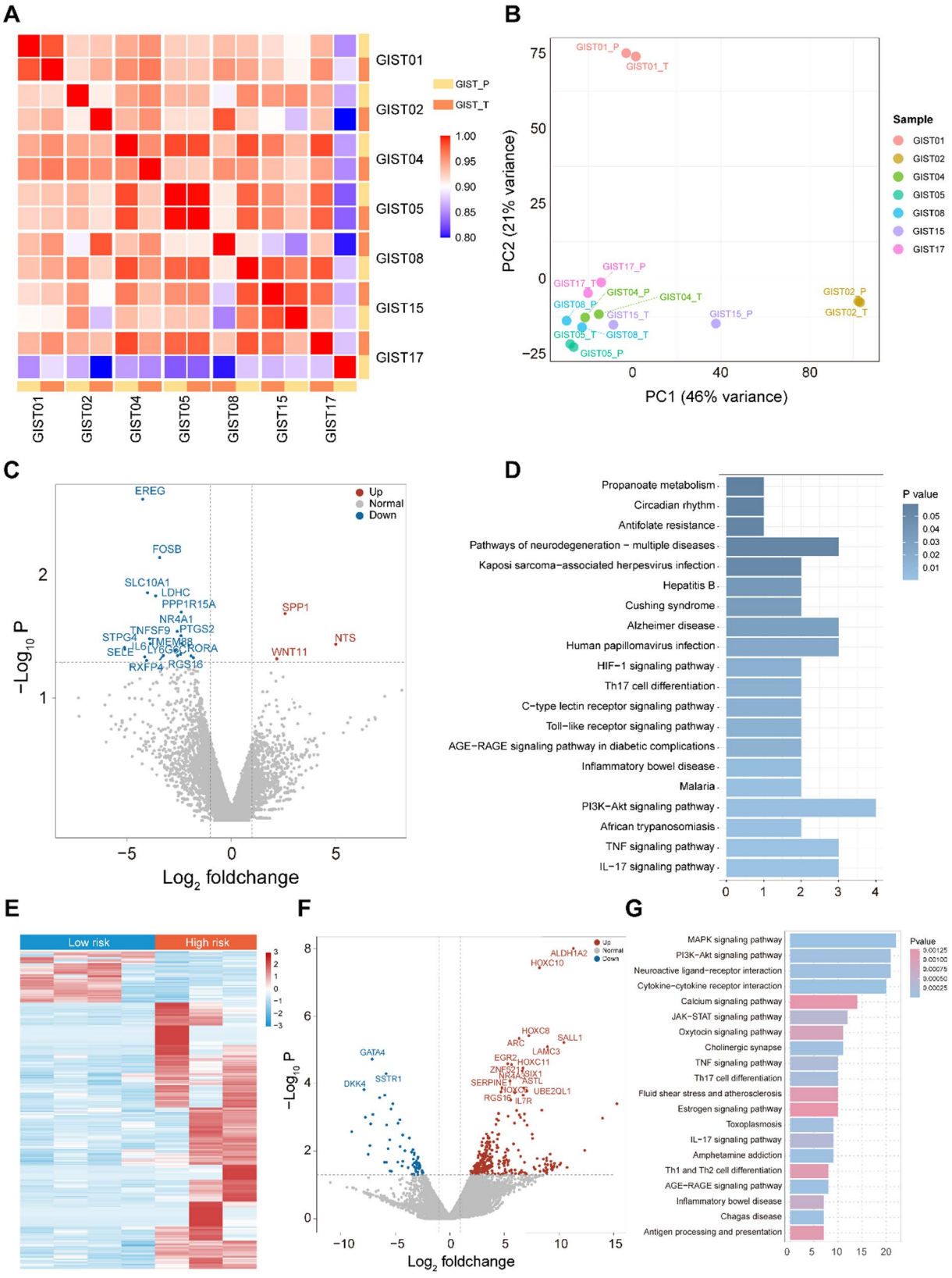

Fig. 4 (See legend on next page.)

(See figure on previous page.)

Fig. 4 3DP-GIST model and transcriptomic characterization of parental tumor tissues. A. Heatmap of gene expression correlation between 3DP-GIST and parental tumor (Pearson correlation). **B**. Principal component analysis (PCA) presents transcriptome data for 3DP-GISTs and corresponding tumor tissues. **C**. Volcano plot illustrating differentially expressed genes between 3DP-GIST models and their corresponding parental tumor specimens. (p value < 0.05, $\log_2$ foldchange ≥ 1). **D**. KEGG pathway enrichment of differential gene expression profiles in the 3DP-GIST model compared to parental tumors. **E**. Heatmap of differentially expressed genes in the high risk of recurrence group ($n = 3$) compared to 3DP-GISTs with low risk of recurrence ($n = 4$). The colored bar represents the $\log_2$-transformed values. **F**. This volcano plot shows the differentially expressed genes in the high recurrence risk and low recurrence risk 3DP-GIST groups. Significantly expressed differential genes are labeled. ($p < 0.05$, $\log_2$ fold change ≥ 1). **G**. KEGG pathway enrichment of differential gene expression profiles in the high recurrence risk 3DP-GISTs compared to low recurrence risk group

gene expression patterns were highly preserved during culture (Fig. 4A). Principal component analysis (PCA) showed that 3DP-GIST was tightly clustered with the corresponding parental tumors (Fig. 4B). While the PCA plots effectively summarize overall variance, some patient samples, such as GIST01 and GIST02, appear somewhat distinct from others, and GIST15_T and GIST15_P are not as tightly clustered as other pairs (Fig. 4B). Such separation can reflect inherent biological heterogeneity between patients or subtle transcriptional adaptations to the ex vivo culture environment. To assess transcriptomic fidelity more granularly, we performed per-patient gene-level correlation analyses. Each 3DP-GIST model exhibited consistently high and significant Pearson correlation coefficients with its matched tumor (Supplementary Fig. S5). These strong correlations at the individual gene level demonstrate that, despite any perceived distance in the aggregated PCA space, the gene expression profiles of our 3DP models consistently maintain high fidelity to their parental tumors, which is crucial for their predictive value.

These results demonstrate that the 3DP-GIST models faithfully retain the transcriptomic profile of the original tumors, highlighting the reproducibility and high fidelity of the model system.

Furthermore, comparative transcriptomic profiling of 3DP-GIST models and their matched primary tumor specimens were undertaken to elucidate pivotal pathways and genes driving tumorigenesis. This analysis identified numerous differentially expressed genes (DEGs) in the 3DP models relative to the parental tumors, underscoring the coexistence of preserved and altered gene expression programs. Notably, the 3DP-GIST models exhibited significant upregulation of *SPP1*, *NTS*, and *WNT11* compared to their parental tumors. These genes have been implicated in various malignancies, contributing to extracellular matrix (ECM) remodeling, tumor stemness, proliferation, and invasion [47–51]. Meanwhile, some epithelial and vascular endothelial as well as energy metabolism-related genes such as EREG, PPP1R15A, and LDHC were down-regulated, which was associated with the lack of vascular in 3DP-GISTs (Fig. 4C) [52–54]. We conducted KEGG pathway enrichment analysis on DEGs between the 3DP-GIST models and their corresponding parental tumors. The analysis revealed significant differences in the PI3K/AKT and TNF signaling pathways (Fig. 4D). These pathways are closely associated with GIST proliferation, invasion, and drug resistance [55, 56]. Notably, SPP1, which was markedly upregulated in the 3DP-GIST models, has been implicated in mediating the activation of both PI3K/AKT and TNF signaling pathways, thereby promoting tumor progression [56–58].

Following our validation of genomic and transcriptomic fidelity, we further investigated whether the 3DP-GIST models also accurately recapitulate the cellular landscape of their parental tumors. Using xCell, a robust computational tool for inferring cell type enrichment from bulk RNA-seq data, we performed deconvolution analysis across 7 paired 3DP-GIST models and original tumor samples.

A heatmap of xCell enrichment scores (Supplementary Fig. S6A) revealed largely consistent cellular composition patterns between the 3DP-GIST models and their matched primary tumors across 64 immune and stromal cell types. Specifically, cell types characteristic of GIST, such as smooth muscle cells and fibroblasts, alongside various immune cell populations, were detected in both model types. A stacked bar plot illustrating the relative proportions of selected major cell types further demonstrated this consistency, showing that the dominant cellular components were generally preserved in the 3DP models (Supplementary Fig. S6B). In contrast, immune cell-related signatures were markedly reduced in the 3DP-GIST models, reflecting the lack of immune infiltration in the ex vivo environment.

Crucially, a Pearson correlation analysis of these xCell scores revealed a strong, statistically significant correlation ($R = 0.97$, $p < 2.2\text{e-}16$) between the 3DP-GIST models and their corresponding parental tumors (Supplementary Fig. S6C). These findings indicate that the 3DP-GIST models preserve the structural and stromal integrity of the tumor microenvironment while reflecting the expected reduction in immune components, thereby reinforcing the physiological relevance of our 3DP-GIST platform.

Taken together, these results indicate that the 3DP-GIST models preserve the majority of the parental tumor's transcriptomic signature while also exhibiting unique transcriptional alterations.

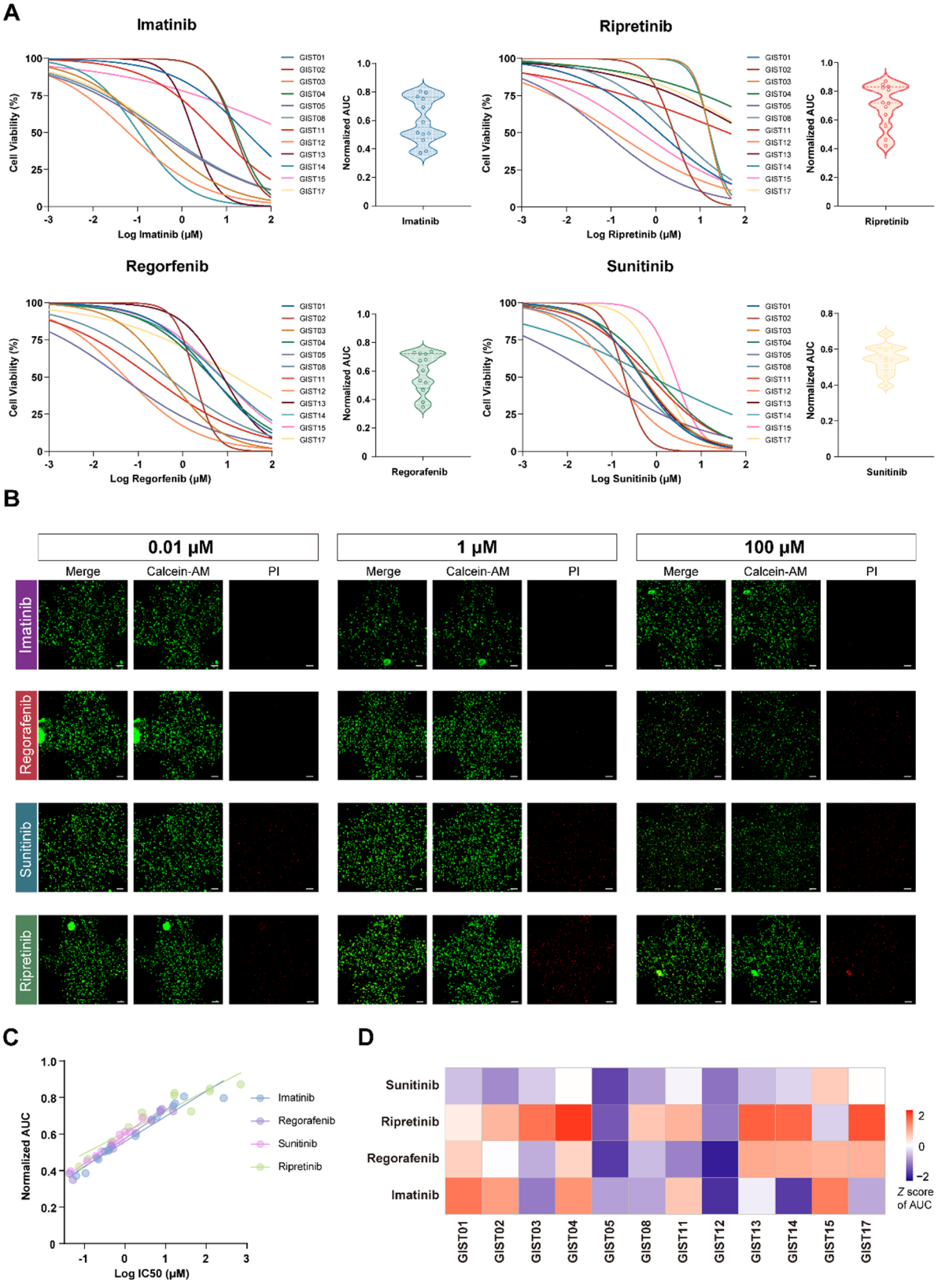

Fig. 5 (See legend on next page.)

(See figure on previous page.)

Fig. 5 3DP-GIST model as a preclinical model for screening targeted drugs. **A.** The dose-response curves demonstrate the sensitivity of the 3DP-GIST model to the four targeted drugs. The violin plot shows normalized AUC values of four targeted drugs in 3DP-GISTs. **B**. Representative Calcein-AM/PI live/dead staining of 3DP-GIST15 after 72 h treatment with four TKIs (Imatinib, Regorafenib, Sunitinib, Ripretinib) at 0.01, 1, and 100 μM. **C**. Scatterplots indicating significant positive correlation between normalized AUC and IC50 values for each of four targeted drugs. **D**. Heatmap illustrating the z-score AUC values of 3DP-GISTs for the four targeted drugs

Gene expression profiles of parental tumor derived 3DP-GIST models with different recurrence risks

We performed RNA sequencing on 3DP-GIST models derived from patients with high and low to intermediate recurrence risks. Heatmap analyses revealed distinct gene expression profiles between the high-risk and low-risk groups (Fig. 4E). Specifically, genes associated with invasion, migration, and cell communication, such as ALDH1A2, LAMC3, SALL1, ARC, HOXC10, PIK3CA, and JUN were significantly upregulated in the high-risk 3DP-GISTs. Conversely, genes linked to the suppression of tumor malignancy, including GATA4, SSTR1, and DKK4, were notably downregulated in the high-risk group compared to the low-risk group (Fig. 4F). KEGG pathway enrichment analysis further supported these findings, indicating that signaling pathways involved in cell proliferation and communication, such as the MAPK signaling pathway, Cytokine-cytokine receptor interaction, PI3K-AKT, and JAK-STAT signaling pathway were significantly enriched in the high-risk 3DP-GIST models (Fig. 4G). These pathways are known to accelerate cell proliferation and maintain intercellular signaling and TME functionality. The activation of these pathways in high-risk 3DP-GISTs underscores their potential role in tumor progression and recurrence.

These observations highlight the utility of 3DP-GIST models in recapitulating the molecular heterogeneity associated with different recurrence risks, providing a valuable platform for studying the mechanisms underlying GIST progression and for evaluating potential therapeutic strategies targeting these signaling pathways.

Drug screening in 3DP-GIST models

To systematically evaluate the preclinical predictive value of the 3DP-GIST platform, we established a molecularly characterized cohort of bioprinted models from 12 GIST specimens (Supplementary Table S2). Clinical-grade TKIs, imatinib (0.01, 0.1, 1, 10, 100 μM), sunitinib (0.01, 0.1, 1, 10, 50 μM), regorafenib (0.01, 0.1, 1, 10, 100 μM) and ripretinib (0.01, 0.1, 1, 10, 50 μM) were administered at therapeutic concentrations in 72-hour dose-escalation experiments, with drug sensitivity quantified via CellTiter-Glo 3D assays. We aim to identify the most sensitive drugs and provide personalized treatment plans for each patient, especially those with recurrence/metastasis or treatment resistance.

Drug efficacy was assessed using half-maximal inhibitory concentration (IC50) values and normalized area under curve (AUC) (Fig. 5A). The 3DP GIST15 model was treated with drugs for 72 h for the cell viability assay. The results showed that the 3DP-GIST model exhibited heterogeneous responses to the drugs, particularly resistance to imatinib and sensitivity to ripretinib. Bright-field microscopy revealed that, following 72 h of treatment with four different targeted therapies, GIST15 cells exhibited pronounced morphological changes, including cellular shrinkage and nuclear fragmentation. Conversely, even under high concentrations of imatinib, GIST015 cells displayed minimal morphological alterations, indicating a resistance to imatinib-induced cytotoxic effects (Supplementary Fig. S7). These results were consistent with those of the CellTiter Glo 3D assay (Fig. 5B).

Notably observed was a significant correlation (Spearman $r^2 > 0.88$) between log IC50 values and AUC between each of the four screened targeted drugs (Fig. 5C). Subsequently, we evaluated the response of the 3DP-GIST model from 12 patients to 4 targeted drugs using the z-score of AUC (Fig. 5D). Screening results revealed significant inter-patient heterogeneity in the responses of patient-derived 3DP-GIST models to the tested agents (Supplementary Fig. S8). Apart from imatinib (the standard first-line targeted therapy for GIST), the majority of models exhibited sensitivity to sunitinib. These findings suggest that sunitinib could be considered the preferred targeted therapy for GIST patients who develop resistance to imatinib in future clinical practice. Interestingly, apart from models GIST05 and GIST12 (which were sensitive to all four selected targeted therapies), all other 3DP-GIST models exhibited varying degrees of resistance to ripretinib. Collectively, these results demonstrate that the 3DP-GIST model is a promising platform for drug screening, exhibiting distinct responses to various targeted therapies.

3DP-GIST model responds to Imatinib treatment

Following established methodologies, we ranked all standardized AUC values from the drug sensitivity assays in descending order. Patients exhibiting clinical disease control defined as partial response (PR) or stable disease (SD), and those with progressive disease (PD) were classified using the Jenks natural breaks optimization algorithm, which identifies natural groupings within data by minimizing intra-class variance and maximizing inter-class variance. This approach delineated the 3DP-GIST models into imatinib-sensitive and imatinib-resistant groups, with an AUC cutoff value of 0.61 (Supplementary

Fig. S9). Subsequent comparative analysis of gene expression profiles between the sensitive and resistant groups revealed distinct differentially expressed genes associated with imatinib response (Fig. 6A). In imatinib-resistant 3DP-GIST models, we observed striking upregulation of *EDIL3*, *SALL4*, and *MAPT*, each previously implicated in driving tumor proliferation and epithelial mesenchymal transition (EMT). Likewise, the resistance-associated genes *TNC* and *PRL* were elevated in these models. By contrast, imatinib-sensitive constructs exhibited significant overexpression of apoptosis- and growth-inhibitory genes (*WDR72*, *SLCO4C1*, *PCDH9*, *CEACAM1*, *DKK1*, and *GP2*) (Fig. 6B). KEGG pathway enrichment results showed that the imatinib-resistant group exhibited significant upregulation of the PI3K-AKT pathway (Fig. 6C). Interestingly, numerous investigations have revealed that the PI3K-AKT signaling pathway is critical for GIST invasiveness and imatinib resistance, a finding that aligns with our sequencing analysis [59–61]. These results underscore the capability of 3DP-GIST models to reflect clinically relevant molecular differences in drug responsiveness.

Patient-specific sensitivity of the 3DP-GIST model for predicting individualized treatment

As previously described, five patients received neoadjuvant tyrosine kinase inhibitor (TKI) therapy, while two received only postoperative adjuvant therapy. Patient GIST01 presented with a recurrent, high-risk GIST showing evidence of drug resistance. Seven years ago, an abdominal mass was detected in GIST01, suspected to be GIST, and surgical resection was performed (Fig. 7A).

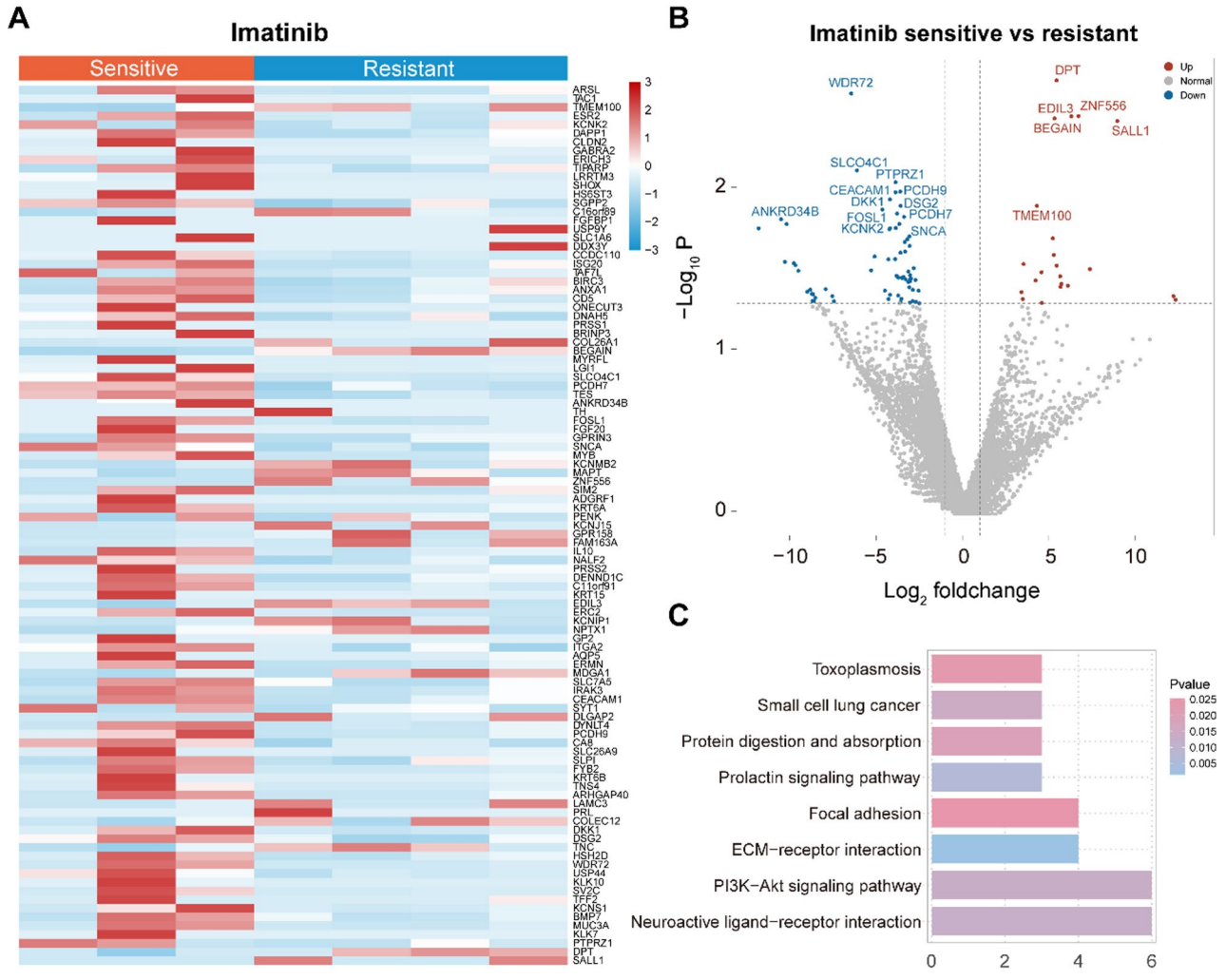

Fig. 6 Characteristic gene expression profiles of 3DP-GISTs with different responses to imatinib. **A.** Heatmap of differentially expressed genes of 3DP-GISTs ($n=4$) in the imatinib-sensitive ($n=3$) compared to imatinib resistance ($n=4$). The colored bar represents the $\log_2$-transformed values. **B**. This volcano plot shows the differentially expressed genes in the imatinib-sensitive ($n=3$) compared to imatinib resistance ($n=4$). Significantly expressed differential genes are labeled. ($p<0.05$, $\log_2$ fold change ≥ 1). **C**. KEGG pathway enrichment of differential gene expression profiles of 3DP-GISTs in the imatinib-sensitive ($n=3$) compared to imatinib-resistance ($n=4$)

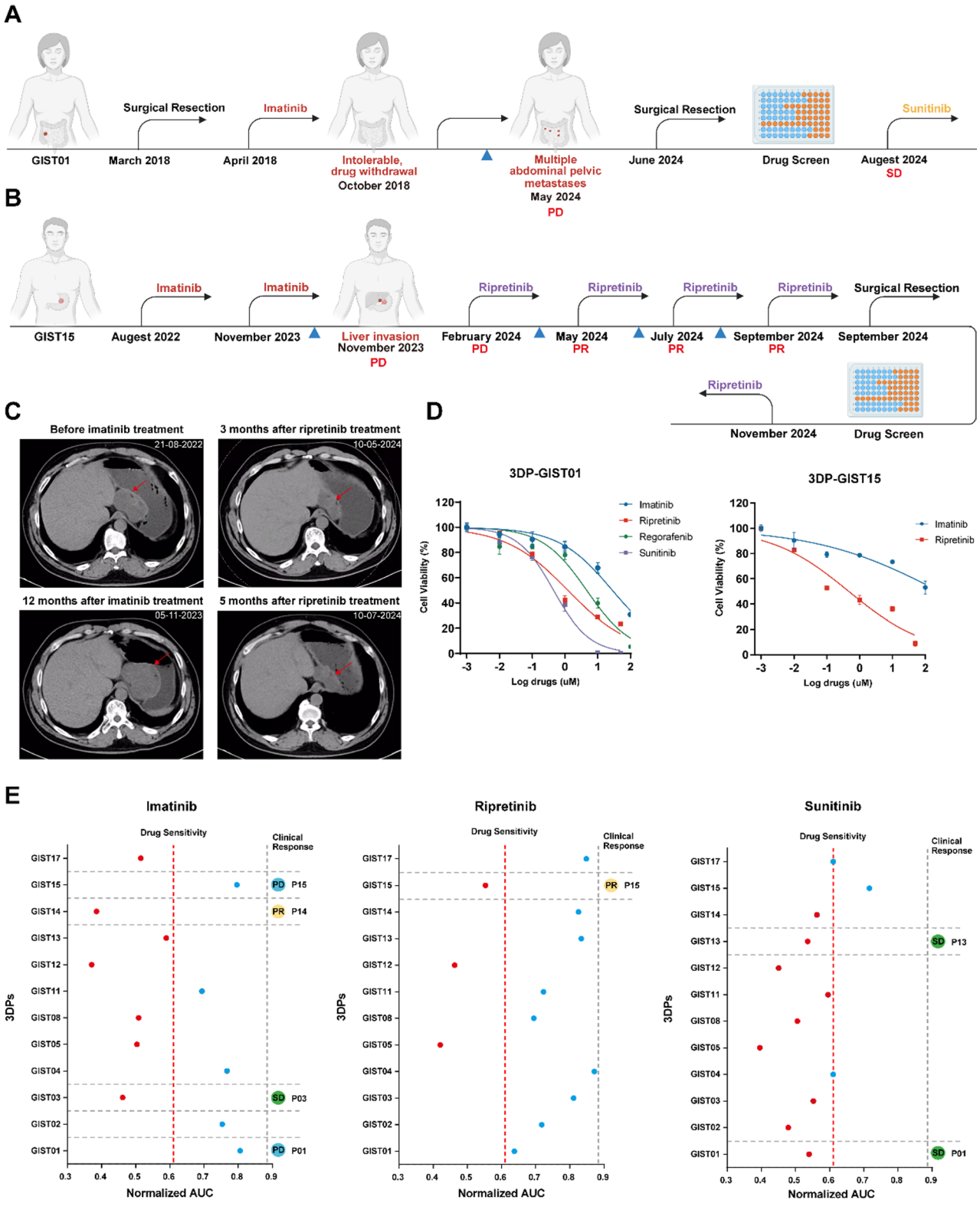

Fig. 7 (See legend on next page.)

(See figure on previous page.)

Fig. 7 3DP-GIST models demonstrate exceptional predictive accuracy for personalized therapy in GIST patients. **A.** Treatment process and clinical response of patient GIST01. The blue arrow indicates when imaging was performed. SD: stable disease. PD: disease progression. **B**. Treatment process and clinical response of patient GIST15. The blue arrow indicates that imaging was performed at this time point. SD: Stable Disease. PD: disease progression. PR: partial response. **C**. The imaging findings of the target lesions in patient GIST15 before and after treatment with two different TKI drugs, including lesion progression after imatinib and lesion regression after ripretinib. **D**. Drug-dose response curves for in vitro screening of four targeted drugs in patient GIST01 and in vitro validation of the efficacy of two drugs in patient GIST15. **E**. For GIST patients receiving TKI targeted therapy, a single scatter plot shows the AUC values determined by drug screening through matching 3D-GISTs. The right side of the plot indicates the patients' clinical responses for consistency in comparison. PR: partial response, PD: disease progression, and SD: stable disease

The patient was subsequently treated with imatinib for six months, but treatment was discontinued due to intolerance. At follow-up last year, recurrent disease with multiple intraperitoneal and pelvic metastases (maximum lesion size 4.8 × 4.3 cm) was identified. A second surgical resection was then carried out, and postoperative pathology confirmed a wild-type GIST with no KIT or PDGFRA mutations detected. A 3DP tumor model was established from the resected specimen and subjected to in vitro drug sensitivity testing. This assay revealed exclusive sensitivity to sunitinib. Accordingly, sunitinib therapy was initiated two months after surgery. Under sunitinib treatment, significant tumor regression was observed, and the disease has since remained stable. These findings demonstrate concordance between the 3DP model's predicted drug sensitivity and the patient's observed clinical response to sunitinib.

GIST15 was derived from a patient with a gastric fundus GIST classified as high risk for recurrence. After four months of imatinib therapy, imaging revealed a marked increase in tumor volume, accompanied by gastric mucosal erosion, ulceration, and invasion of the liver and diaphragm, indicating primary imatinib resistance (Fig. 7B). The patient was then treated with ripretinib for six months, leading to pronounced tumor shrinkage; although a transient rebound in tumor size occurred mid-treatment, the tumor ultimately continued to decrease and met criteria for surgical resection (Fig. 7C). Subsequently, a patient-derived 3DP-GIST model (GIST15) was established and subjected to drug sensitivity testing. Consistent with the patient's clinical response, the model exhibited resistance to imatinib and relative sensitivity to ripretinib and sunitinib (Fig. 7D).

Patient GIST14 presented with a gastric GIST (8.2 × 7.2 cm) that demonstrated progressive response to neoadjuvant imatinib (400 mg/d): 14.6% reduction at month 1 (7.1 × 6.5 cm) and 42.7% cumulative shrinkage by month 5 (6.0 × 5.0 cm). Post-resection 3DP model revealed high imatinib sensitivity (AUC = 0.38) below the predefined clinical cutoff (AUC = 0.61), validating the platform's capacity to quantify therapeutic response gradients (Fig. 7D, Supplementary Fig. S10).

Furthermore, we focused on 5 patients who had undergone TKI therapy, comparing the drug sensitivity results from patient-derived 3DP-GIST models with their corresponding clinical responses (Fig. 7E). The treatments included imatinib ($n = 4$), ripretinib ($n = 1$), and sunitinib ($n = 2$). Among the four patients treated with imatinib, two (GIST01 and GIST15) experienced PD, one (GIST03) achieved SD, and one (GIST14) achieved a PR. Notably, the drug sensitivity testing results from the 3DP-GIST models aligned with these clinical outcomes. Specifically, the models corresponding to patients with SD and PR exhibited AUC values below the established cutoff of 0.61, with the model from GIST14 (PR) showing the lowest AUC. Conversely, models from patients with PD had AUC values above the cutoff, indicating resistance. Similar correlations were observed with sunitinib and ripretinib treatments. These findings underscore the predictive value of 3DP-GIST models in assessing patient-specific drug responses, potentially guiding personalized treatment strategies.

Discussion

Therapeutic resistance to TKIs and heterogeneity represent pivotal challenges in managing advanced and metastatic GIST, contributing to a mPFS of merely 5.1 months in refractory cases [62, 63]. Recent studies have identified multiple mechanisms of resistance, including heterogeneous primary and secondary KIT mutations and reactivation of KIT signaling via polyclonal mutant clones, compensatory activation of bypass signaling pathways and TME remodeling [64–68]. Despite these insights, critical clinical dilemmas persist, after the development of imatinib resistance, options for precision therapy are scarce, and strategies to maximize clinical benefit are urgently needed. Currently, there is a dearth of robust biomarkers and predictive tools for patient stratification and outcome forecasting in GIST. Furthermore, existing in vitro cell models fail to capture the complexity of the GIST tumor microenvironment and exhibit limited fidelity to patient tumors. To address these unmet needs, we propose to develop patient-derived 3DP-GIST model as a high-throughput preclinical platform to guide personalized treatment strategies for advanced GIST.

3D bioprinting has emerged as a transformative platform for constructing patient-derived tumor models and advancing drug screening, characterized by rapid fabrication, high reproducibility, and robust clinical translatability [69, 70].

By leveraging programmable, computer-aided extrusion systems, researchers can fabricate complex tumor

constructs in hours, reducing manual handling and ensuring consistent outcomes across batches. The incorporation of tailored hydrogel bioinks provides tunable mechanical properties and biochemical cues that more faithfully recapitulate the TME, reflecting the biological complexity and heterogeneity of solid tumors [71, 72]. These bioprinted models outperform traditional 2D cultures and organoids in predictive accuracy and cost-effectiveness, establishing themselves as reliable preclinical platforms for personalized oncology [73, 74].

To date, no reliable in vitro drug-sensitivity assay for GIST has been reported, severely hampering treatment strategies and prognosis for patients with recurrent, metastatic, or drug-resistant disease. In this study, we leveraged 3D bioprinting to encapsulate patient-derived GIST cells within a GelMA/HAMA composite hydrogel, successfully establishing 12 distinct 3DP-GIST models. These constructs faithfully recapitulated the intertumoral heterogeneity and demonstrated high concordance with their parental tumors in morphology, histopathology, and molecular signature. Furthermore, beyond molecular profiling, our comprehensive xCell analysis revealed a strong correlation in cell type composition between the 3DP-GIST models and their parental tumors (Supplementary Fig. S6A-C). This finding suggests that our models substantially preserve the complex cellular landscape of the original tumors, including various immune and stromal cell populations, which are critical components influencing tumor biology and drug response. While our current mono-culture 3DP system may not fully recapitulate the dynamic functional interactions of all immune cells or the complete heterogeneity of the in vivo tumor microenvironment, the demonstrated preservation of overall cellular composition significantly enhances the physiological relevance of our models.

Furthermore, to provide direct functional validation at the protein level, we performed Western blot analyses of the crucial KIT downstream signaling pathway. Our results unequivocally demonstrate that the activation status of KIT, AKT, and ERK1/2, as indicated by their phosphorylation levels, is faithfully maintained in the 3DP-GIST models, closely mirroring that in their corresponding parental tumors (Supplementary Fig. S3). This biochemical fidelity reinforces the robustness of our models and their capability to preserve the key oncogenic drivers of GIST, providing a reliable platform for studying targeted therapy mechanisms.

In the absence of effective therapies for recurrent, metastatic, or mutation-negative GISTs, our 3DP-GIST platform offers a much-needed tool for rapid tumor modeling, high-throughput drug screening, and preclinical evaluation across early and advanced disease settings.

While imatinib remains the first-line therapy for GISTs harboring KIT or PDGFRA mutations, resistance to this treatment poses a significant clinical challenge. Approximately 15–20% of patients exhibit primary resistance, and most patients who initially respond develop secondary resistance within 18–24 months of therapy. Secondary resistance is often associated with the emergence of additional KIT mutations, particularly in exons 13, 14, or 17, leading to disease progression despite continued treatment [75, 76]. To address imatinib resistance, second-line and third-line therapies such as sunitinib and regorafenib have been developed. Sunitinib, approved for patients who progress on or are intolerant to imatinib, has demonstrated a median progression-free survival (PFS) of approximately 5.6 months. Regorafenib, used as a third-line therapy, offers a mPFS of around 4.8 months. More recently, ripretinib, a novel switch-control tyrosine kinase inhibitor, has been approved for patients who have received three or more prior kinase inhibitors. In the INVICTUS phase III trial, ripretinib significantly improved mPFS to 6.3 months compared to 1.0 month with placebo [77]. Although ripretinib did not demonstrate superiority over sunitinib in the second-line setting in the INTRIGUE trial, it exhibited a comparable PFS and a more favorable safety profile, suggesting it may be a suitable alternative for certain patients [78]. Despite these advancements, overcoming imatinib resistance remains a major hurdle in the management of GISTs. Ongoing research into the molecular mechanisms underlying resistance and the development of more effective targeted therapies are essential to improve outcomes for patients with advanced GISTs [6].

We utilized patient-derived tumor tissues to construct 3DP-GIST models for personalized drug screening. Applying a previously established method, we classified normalized AUC values to determine a resistance-sensitivity threshold (AUC = 0.61) [20, 31]. Our results demonstrated that the drug response profiles of the 3DP-GISTs corresponded closely with actual clinical outcomes. Notably, patient GIST01, diagnosed with wild-type and recurrent GIST, exhibited intolerance and resistance to imatinib during treatment. Postoperative construction and drug sensitivity testing of the patient's 3DP-GIST model revealed a favorable response to sunitinib. Subsequent adjuvant therapy with sunitinib led to stable disease control. Similarly, patient GIST15 showed imatinib resistance during neoadjuvant therapy. Clinical administration of ripretinib resulted in tumor reduction and disease remission, as evidenced by imaging studies. Consistently, among the four targeted therapies tested, the 3DP-GIST model for this patient responded exclusively to ripretinib.

While our 3DP-GIST models represent a significant advance over traditional 2D cultures by offering a more physiologically relevant microenvironment, it is crucial to acknowledge certain limitations in fully recapitulating

the complexity of the in vivo TME. Current mono-culture 3DP systems, including ours, may not dynamically simulate all aspects such as the intricate interplay with diverse immune cell populations, specific oxygen gradients, complex metabolite exchange, and the dynamic signaling from peripheral nerves or endothelial cells within the tumor [79]. These factors, while challenging to integrate, are known to influence tumor biology and drug response. Future iterations of 3DP-GIST models will aim to incorporate more complex co-culture systems and advanced bioinks to further enrich the TME fidelity. Another limitation of the present study is the relatively small cohort size and partial availability of WES data, which may lead to cohort-specific differences in mutation frequencies compared with larger studies. Nevertheless, the mutational profiles of our samples are consistent with the general genomic landscape of GISTs, and each 3DP-GIST model retained the same driver variants as its corresponding tumor, supporting the stability and fidelity of the platform. Future work with expanded cohorts and longitudinal sampling will be necessary to robustly assess clonal evolution and treatment selection in 3DP-GIST models.

These findings indicate that 3DP-GIST models can accurately reflect individual patient drug responses, facilitating the identification of effective treatment regimens. Moreover, the entire process-from model construction to drug sensitivity testing can be completed within 8 to 10 days, significantly shortening the therapeutic decision-making window and potentially improving patient prognoses.

Conclusion

In summary, our study establishes patient-derived 3DP-GIST models as a promising preclinical platform for personalized therapy, addressing the current lack of suitable in vitro models for individualized drug response prediction in GIST. These 3DP-GIST models accurately recapitulate the histological architecture, genomic mutation landscape, and gene expression profiles of the original tumors. They enable in-depth mechanistic investigations into GIST recurrence and imatinib resistance, facilitate the development a predictive evaluation of novel therapeutic strategies, and establish a robust foundation for future precision medicine initiatives.

This research underscores the potential of 3DP-based methodologies in oncology and molecular medicine, offering new avenues for understanding and treating this challenging disease. Future studies should focus on establishing a larger cohort of 3DP-GIST models to validate and refine our findings. Integrating the 3DP-GIST platform with comprehensive genomic sequencing will further enhance the reliability and applicability of research outcomes.

Abbreviations

GIST	Gastrointestinal stromal tumor
TME	Tumor microenvironment
3DP	Three-dimensional bioprinting
WES	Whole-exome sequencing
mPFS	median progression-free survival
NGS	Next generation sequencing
GelMA	Gelatin methacryloyl (GelMA)
HAMA	hyaluronic acid methacryloyl
ECM	Extracellular matrix
H&E	Hematoxylin and eosin
IHC	Immunohistochemistry
AUC	Area under curve

Supplementary Information

The online version contains supplementary material available at https://doi.org/10.1186/s12951-025-03934-6.

Supplementary Material 1.

Acknowledgements

The authors express sincere gratitude to all patients who provided informed consent for tissue donation to support this research. We would like to extend our gratitude to the Biomedical Engineering Facility of National Infrastructures for Translational Medicine at PUMCH.

Author contributions

L.D. conducted experiments, and wrote the manuscript. Y.M., H.Y. and W.K., conceived, designed, and supervised the study, obtained funding and provided administrative, technical, or material support. Z.Z, Y.H. and W.K. prepared and processed the clinical samples. Z.K, Y.L., H.S., M.S., M.P. and S.J. collected the patient's information. L.D., H.Y., Y.M., Y.W., S.D., H.Z. conceived the study. L.D., Y.W., and H.Y. supervised the process of the study and revised the manuscript.

Funding

This work was supported by the National Natural Science Foundation of China (82472174, 32271470), Noncommunicable Chronic Diseases-National Science and Technology Major Project (2024ZD0520602), Beijing Natural Science Foundation (7232117), CAMS Innovation Fund for Medical Sciences (2023-I2M-C&T-B-016).

Data availability

The sequencing data reported in this paper have been deposited in the Genome Sequence Archive for Humans (https://ngdc.cncb.ac.cn/gsa-human/) under accession number HRA014874 and will be made publicly available upon the publication date. The data that support the findings of this study are available from the corresponding author upon reasonable request.

Declarations

Ethics approval and consent to participate

This study was approved by the Ethics Review Committee of Peking Union Medical College Hospital (Approval No. I-25PJ0659). All procedures adhered to the ethical guidelines of the Declaration of Helsinki and the International Conference on Harmonisation's Good Clinical Practice. Histopathological postoperative analysis was conducted to verify the presence of GIST in all participants, and written informed consent was obtained from each subject prior to study enrollment.

Consent for publication

Not applicable.

Competing interests

The authors declare no competing interests.

Author details

[1]Department of Liver Surgery, Peking Union Medical College (PUMC) Hospital, Peking Union Medical College (PUMC), Chinese Academy of

Medical Sciences (CAMS), 1# Shuai-Fu-Yuan, Wang-Fu-Jing, Beijing 100730, China
[2]Department of General Surgery, Peking Union Medical College Hospital, Chinese Academy of Medical Science and Peking Union Medical College, 1# Shuai-Fu-Yuan, Wang-Fu-Jing, Beijing, Beijing 100730, China
[3]State Key Laboratory of Common Mechanism Research for Major Diseases, Haihe Laboratory of Cell Ecosystem, Department of Physiology, Institute of Basic Medical Sciences, School of Basic Medicine, Chinese Academy of Medical Sciences and Peking Union Medical College, Beijing, China

Received: 25 August 2025 / Accepted: 7 December 2025
Published online: 18 December 2025

References

1. Casali P, Abecassis N, Bauer S, Biagini R, Bielack S, Bonvalot S, et al. Gastrointestinal stromal tumours: ESMO–EURACAN clinical practice guidelines for diagnosis, treatment and follow-up. Ann Oncol. 2018;29:iv68–78.
2. Søreide K, Sandvik OM, Søreide JA, Giljaca V, Jureckova A, Bulusu VR. Global epidemiology of Gastrointestinal stromal tumours (GIST): a systematic review of population-based cohort studies. Cancer Epidemiol. 2016;40:39–46.
3. Serrano C, George S. Gastrointestinal stromal tumor: challenges and opportunities for a new decade. Clin Cancer Res. 2020;26:5078–85.
4. Blay J-Y, Kang Y-K, Nishida T, von Mehren M. Gastrointestinal stromal tumours. Nat Rev Dis Primers. 2021;7:22.
5. Schaefer I-M, DeMatteo RP, Serrano C. The GIST of advances in treatment of advanced gastrointestinal stromal tumor. In *American Society of Clinical Oncology educational book American Society of Clinical Oncology Annual Meeting*. 2022: 1.
6. Klug LR, Khosroyani HM, Kent JD, Heinrich MC. New treatment strategies for advanced-stage Gastrointestinal stromal tumours. Nat Rev Clin Oncol. 2022;19:328–41.
7. Martin-Broto J, Moura DS. New drugs in Gastrointestinal stromal tumors. Curr Opin Oncol. 2020;32:314–20.
8. Symcox M, Jones RL. Ripretinib versus sunitinib in patients with advanced Gastrointestinal stromal tumor after treatment with imatinib: a plain language summary of the phase 3 INTRIGUE trial. Future Oncol. 2023;19:2383–93.
9. Meric-Bernstam F, Johnson A, Holla V, Bailey AM, Brusco L, Chen K, et al. A decision support framework for genomically informed investigational cancer therapy. J Natl Cancer Inst. 2015;107:djv098.
10. Beltran H, Eng K, Mosquera JM, Sigaras A, Romanel A, Rennert H, Kossai M, Pauli C, Faltas B, Fontugne J. Whole-exome sequencing of metastatic cancer and biomarkers of treatment response. JAMA Oncol. 2015;1:466–74.
11. Dermawan JK, Kelly C, Gao Z, Smith S, Jadeja B, Singer S, et al. Novel genomic risk stratification model for primary gastrointestinal stromal tumors (GIST) in the adjuvant therapy era. Clin Cancer Res. 2023;29:3974–85.
12. Calderillo-Ruíz G, Pérez-Yepez EA, García-Gámez MA, Millan-Catalan O, Díaz-Romero C, Ugalde-Silva P, et al. Genomic profiling in GIST: implications in clinical outcome and future challenges. Neoplasia. 2024;48:100959.
13. Tuveson D, Clevers H. Cancer modeling meets human organoid technology. Science. 2019;364:952–5.
14. Sleeboom JJ, van Tienderen GS, Schenke-Layland K, van der Laan LJ, Khalil AA, Verstegen MM. The extracellular matrix as hallmark of cancer and metastasis: from biomechanics to therapeutic targets. Sci Transl Med. 2024;16:eadg3840.
15. Neufeld L, Yeini E, Pozzi S, Satchi-Fainaro R. 3D bioprinted cancer models: from basic biology to drug development. Nat Rev Cancer. 2022;22:679–92.
16. Tang M, Jiang S, Huang X, Ji C, Gu Y, Qi Y, et al. Integration of 3D bioprinting and multi-algorithm machine learning identified glioma susceptibilities and microenvironment characteristics. Cell Discovery. 2024;10:39.
17. Wang X, Zhang X, Dai X, Wang X, Li X, Diao J, et al. Tumor-like lung cancer model based on 3D bioprinting. 3 Biotech. 2018;8:1–9.
18. Sun H, Wang Y, Sun M, Ke X, Li C, Jin B, Pang M, Wang Y, Jiang S, Du L. Developing Patient-Derived 3D-Bioprinting models of pancreatic cancer. J Adv Res. 2025;74:165–74.
19. Xie F, Sun L, Pang Y, Xu G, Jin B, Xu H, Lu X, Xu Y, Du S, Wang Y. Three-dimensional bio-printing of primary human hepatocellular carcinoma for personalized medicine. Biomaterials. 2021;265:120416.
20. Sun H, Sun L, Ke X, Liu L, Li C, Jin B, et al. Prediction of clinical precision chemotherapy by patient-derived 3D bioprinting models of colorectal cancer and its liver metastases. Adv Sci (Weinh). 2024;11:2304460.
21. Gao T, He X, Wang J, Liu J, Hu X, Bai C, et al. Self-assembled patient-derived tumor-like cell clusters for personalized drug testing in diverse sarcomas. Cell Rep Med. 2025. https://doi.org/10.1016/j.xcrm.2025.101990
22. Al Shihabi A, Tebon PJ, Nguyen HTL, Chantharasamee J, Sartini S, Davarifar A, et al. The landscape of drug sensitivity and resistance in sarcoma. Cell Stem Cell. 2024;31:1524-1542. e1524.
23. Jung DJ, Byeon JH, Kim YC, Jeong WS, Choi J-W, Jeong GS. Generation of sarconoids from angiosarcoma patients as a systematic-based rational approach to treatment. J Hematol Oncol. 2024;17:35.
24. Shen R, Seshan VE. FACETS: allele-specific copy number and clonal heterogeneity analysis tool for high-throughput DNA sequencing. Nucleic Acids Res. 2016;44:e131-e131.
25. Sahraeian SME, Mohiyuddin M, Sebra R, Tilgner H, Afshar PT, Au KF, Bani Asadi N, Gerstein MB, Wong WH, Snyder MP. Gaining comprehensive biological insight into the transcriptome by performing a broad-spectrum RNA-seq analysis. Nat Commun. 2017;8:59.
26. Aran D, Hu Z, Butte AJ. xCell: digitally portraying the tissue cellular heterogeneity landscape. Genome Biol. 2017;18:220.
27. Eisenhauer EA, Therasse P, Bogaerts J, Schwartz LH, Sargent D, Ford R, Dancey J, Arbuck S, Gwyther S, Mooney M. New response evaluation criteria in solid tumours: revised RECIST guideline (version 1.1). Eur J Cancer. 2009;45:228–47.
28. Luo Y, Chen J, Huang K, Lin Y, Chen M, Xu L, Li Z-P, Feng S-T. Early evaluation of Sunitinib for the treatment of advanced gastroenteropancreatic neuroendocrine neoplasms via CT imaging: RECIST 1.1 or Choi criteria? BMC Cancer. 2017;17:1–10.
29. Choi H, Charnsangavej C, Faria SC, Macapinlac HA, Burgess MA, Patel SR, Chen LL, Podoloff DA, Benjamin RS. Correlation of computed tomography and positron emission tomography in patients with metastatic Gastrointestinal stromal tumor treated at a single institution with Imatinib mesylate: proposal of new computed tomography response criteria. J Clin Oncol. 2007;25:1753–9.
30. Jenks GF. Optimal data classification for choropleth maps. *Department of Geographiy, University of Kansas Occasional Paper* 1977.
31. Grossman JE, Muthuswamy L, Huang L, Akshinthala D, Perea S, Gonzalez RS, Tsai LL, Cohen J, Bockorny B, Bullock AJ. Organoid sensitivity correlates with therapeutic response in patients with pancreatic cancer. Clin Cancer Res. 2022;28:708–18.
32. Yang H, Sun L, Pang Y, Hu D, Xu H, Mao S, Peng W, Wang Y, Xu Y, Zheng Y-C. Three-dimensional bioprinted hepatorganoids prolong survival of mice with liver failure. Gut. 2021;70:567–74.
33. Deng B, Ma Y, Huang J, He R, Luo M, Mao L, et al. Revitalizing liver function in mice with liver failure through transplantation of 3D-bioprinted liver with expanded primary hepatocytes. Sci Adv. 2024;10:eado1550.
34. Joensuu H, Vehtari A, Riihimäki J, Nishida T, Steigen SE, Brabec P, Plank L, Nilsson B, Cirilli C, Braconi C. Risk of recurrence of Gastrointestinal stromal tumour after surgery: an analysis of pooled population-based cohorts. Lancet Oncol. 2012;13:265–74.
35. O'Connell C, Onofrillo C, Duchi S, Li X, Zhang Y, Tian P, Lu L, Trengove A, Quigley A, Gambhir S. Evaluation of sterilisation methods for bio-ink components: gelatin. 2019.
36. Souness A, Zamboni F, Walker GM, Collins MN. Influence of scaffold design on 3 D printed cell constructs. J Biomedical Mater Res Part B: Appl Biomaterials. 2018;106:533–45.
37. Yue K, Trujillo-de Santiago G, Alvarez MM, Tamayol A, Annabi N, Khademhosseini A. Synthesis, properties, and biomedical applications of gelatin methacryloyl (GelMA) hydrogels. Biomaterials. 2015;73:254–71.
38. Zhang Y, Wang Z, Hu Q, Luo H, Lu B, Gao Y, et al. 3D bioprinted GelMA-nanoclay hydrogels induce colorectal cancer stem cells through activating wnt/β-catenin signaling. Small. 2022;18:2200364.
39. Zhang Y, Hu Q, Pei Y, Luo H, Wang Z, Xu X, Zhang Q, Dai J, Wang Q, Fan Z. A patient-specific lung cancer assembloid model with heterogeneous tumor microenvironments. Nat Commun. 2024;15:3382.
40. Tang M, Xie Q, Gimple RC, Zhong Z, Tam T, Tian J, Kidwell RL, Wu Q, Prager BC, Qiu Z. Three-dimensional bioprinted glioblastoma microenvironments model cellular dependencies and immune interactions. Cell Res. 2020;30:833–53.
41. Zhao Y, Li S, Zhu L, Huang M, Xie Y, Song X, et al. Personalized drug screening using patient-derived organoid and its clinical relevance in gastric cancer. Cell Rep Med. 2024;5:101627.

42. Alexandrov LB, Kim J, Haradhvala NJ, Huang MN, Tian Ng AW, Wu Y, Boot A, Covington KR, Gordenin DA, Bergstrom EN. The repertoire of mutational signatures in human cancer. Nature. 2020;578:94–101.
43. Tate JG, Bamford S, Jubb HC, Sondka Z, Beare DM, Bindal N, Boutselakis H, Cole CG, Creatore C, Dawson E. COSMIC: the catalogue of somatic mutations in cancer. Nucleic Acids Res. 2019;47:D941–7.
44. Feng Y, Yao S, Pu Z, Cheng H, Fei B, Zou J, et al. Identification of new tumor-related gene mutations in Chinese gastrointestinal stromal tumors. Front Cell Dev Biol. 2021;9:764275.
45. Li P, Li M, Wang K, Liu Y, Wang Y, Zhao D, et al. Genetic alterations in cell cycle regulation-associated genes may promote primary progression of gastrointestinal stromal tumors. Lab Invest. 2020;100:426–37.
46. Xie F, Luo S, Liu D, Lu X, Wang M, Liu X, et al. Genomic and transcriptomic landscape of human gastrointestinal stromal tumors. Nat Commun. 2024;15:9495.
47. Nallasamy P, Nimmakayala RK, Karmakar S, Leon F, Seshacharyulu P, Lakshmanan I, Rachagani S, Mallya K, Zhang C, Ly QP. Pancreatic tumor microenvironment factor promotes cancer stemness via SPP1–CD44 axis. Gastroenterology. 2021;161:1998–2013. e1997.
48. Hung Y-H, Wang H-C, Hsu S-H, Wang L-Y, Tsai Y-L, Su Y-Y, Hung W-C, Chen L-T. Neuron-derived neurotensin promotes pancreatic cancer invasiveness and gemcitabine resistance via the NTSR1/Akt pathway. Am J Cancer Res. 2024;14:448.
49. Rodriguez-Hernandez I, Maiques O, Kohlhammer L, Cantelli G, Perdrix-Rosell A, Monger J, Fanshawe B, Bridgeman VL, Karagiannis SN, Penin RM. WNT11-FZD7-DAAM1 signalling supports tumour initiating abilities and melanoma amoeboid invasion. Nat Commun. 2020;11:5315.
50. Menck K, Heinrichs S, Wlochowitz D, Sitte M, Noeding H, Janshoff A, et al. WNT11/ROR2 signaling is associated with tumor invasion and poor survival in breast cancer. J Exp Clin Cancer Res. 2021;40:1–18.
51. Fujiya K, Ohshima K, Kitagawa Y, Hatakeyama K, Nagashima T, Aizawa D, et al. Aberrant expression of Wnt/β-catenin signaling pathway genes in aggressive malignant gastric gastrointestinal stromal tumors. Eur J Surg Oncol. 2020;46:1080–7.
52. Cui Y, Cao X, Zhang Y, Fu C, Li D, Sun Y, et al. Protein phosphatase 1 regulatory subunit 15 A (PPP1R15A) promoted the progression of gastric cancer by activating cell autophagy under energy stress. J Exp Clin Cancer Res. 2025;44:52.
53. Chen Y, Huo R, Kang W, Liu Y, Zhao Z, Fu W, et al. Tumor-associated monocytes promote mesenchymal transformation through EGFR signaling in glioma. Cell Rep Med. 2023;2023;4(9). https://doi.org/10.1016/j.xcrm.2023.101177
54. Naik A, Thomas R, Al-Khalifa A, Qasem H, Decock J. Immunomodulatory effects of tumor Lactate Dehydrogenase C (LDHC) in breast cancer. Cell Commun Signal. 2025;23:145.
55. Boichuk S, Bikinieva F, Nurgatina I, Dunaev P, Valeeva E, Aukhadieva A, et al. Inhibition of AKT-signaling sensitizes soft tissue sarcomas (STS) and gastrointestinal stromal tumors (GIST) to doxorubicin via targeting of homology-mediated DNA repair. Int J Mol Sci. 2020;21:8842.
56. Cao L, Li Z, Huang Y, Chen H, Chen L, Tao L, et al. Huaier inhibits the proliferation and migration of gastrointestinal stromal tumors by regulating the JAK2/STAT3 signaling pathway. J Ethnopharmacol. 2025, 342:119389. https://doi.org/10.1016/j.jep.2025.119389
57. Liu C, Ge H, Shen C, Hu D, Zhao X, Qin R, Wang Y. NOTCH3 promotes malignant progression of bladder cancer by directly regulating SPP1 and activating PI3K/AKT pathway. Cell Death Dis. 2024;15:840.
58. Qian J, LeSavage BL, Hubka KM, Ma C, Natarajan S, Eggold JT, et al. Cancer-associated mesothelial cells promote ovarian cancer chemoresistance through paracrine osteopontin signaling. J Clin Invest. 2021;131(16) . https://doi.org/10.1172/JCI146186
59. Zhao Y, Weng Z, Zhou X, Xu Z, Cao B, Wang B, et al. Mesenchymal stromal cells promote the drug resistance of gastrointestinal stromal tumors by activating the PI3K-AKT pathway via TGF-β2. J Transl Med. 2023;21:219.
60. Li J, Dang Y, Gao J, Li Y, Zou J, Shen L. PI3K/AKT/mTOR pathway is activated after Imatinib secondary resistance in Gastrointestinal stromal tumors (GISTs). Med Oncol. 2015;32:1–7.
61. Long Z-W, Wu J-H, Wang Y-N, Zhou Y. MiR-374b promotes proliferation and inhibits apoptosis of human GIST cells by inhibiting PTEN through activation of the PI3K/Akt pathway. Mol Cells. 2018;41:532–44.
62. Yang Y, Li S, Wang Y, Zhao Y, Li Q. Protein tyrosine kinase inhibitor resistance in malignant tumors: molecular mechanisms and future perspective. Signal Transduct Target Ther. 2022;7:329.
63. Hemming M, Heinrich M, Bauer S, George S. Translational insights into Gastrointestinal stromal tumor and current clinical advances. Ann Oncol. 2018;29:2037–45.
64. Liegl B, Kepten I, Le C, Zhu M, Demetri G, Heinrich M, Fletcher C, Corless C, Fletcher J. Heterogeneity of kinase inhibitor resistance mechanisms in GIST. J Pathology: J Pathological Soc Great Br Irel. 2008;216:64–74.
65. Zhou S, Abdihamid O, Tan F, Zhou H, Liu H, Li Z, et al. KIT mutations and expression: current knowledge and new insights for overcoming IM resistance in GIST. Cell Commun Signal. 2024;22:153.
66. He C, Wang Z, Yu J, Mao S, Xiang X. Current drug resistance mechanisms and treatment options in gastrointestinal stromal tumors: summary and update. Curr Treat Options Oncol. 2024, 25:1390-1405. . https://doi.org/10.1007/s11864-024-01272-7
67. Ou X, Gao G, Habaz IA, Wang Y. Mechanisms of resistance to tyrosine kinase inhibitor-targeted therapy and overcoming strategies. MedComm. 2024;5:e694.
68. Liu X, Yu J, Li Y, Shi H, Jiao X, Liu X, et al. Deciphering the tumor immune microenvironment of imatinib-resistance in advanced gastrointestinal stromal tumors at single-cell resolution. Cell Death Dis. 2024;15:190.
69. Knowlton S, Onal S, Yu CH, Zhao JJ, Tasoglu S. Bioprinting for cancer research. Trends Biotechnol. 2015;33:504–13.
70. Jung M, Ghamrawi S, Du EY, Gooding JJ, Kavallaris M. Advances in 3D bioprinting for cancer biology and precision medicine: from matrix design to application. Adv Healthc Mater. 2022;11:2200690.
71. Han J, Jeong HJ, Choi J, Kim H, Kwon T, Myung K, et al. Bioprinted patient-derived organoid arrays capture intrinsic and extrinsic tumor features for advanced personalized medicine. Adv Sci. 2025, 12:2407871. https://doi.org/10.1002/advs.202407871
72. Choi Ym, Na D, Yoon G, Kim J, Min S, Yi HG, et al. Prediction of patient drug response via 3D bioprinted gastric cancer model utilized patient-derived tissue laden tissue-specific bioink. Adv Sci. 2025, 12:2411769. https://doi.org/10.1002/advs.202411769
73. Tebon PJ, Wang B, Markowitz AL, Davarifar A, Tsai BL, Krawczuk P, et al. Drug screening at single-organoid resolution via bioprinting and interferometry. Nat Commun. 2023;14:3168.
74. Augustine R, Kalva SN, Ahmad R, Zahid AA, Hasan S, Nayeem A, et al. 3D bioprinted cancer models: revolutionizing personalized cancer therapy. Transl Oncol. 2021;14:101015.
75. Kee D, Zalcberg JR. Current and emerging strategies for the management of imatinib-refractory advanced gastrointestinal stromal tumors. Ther Adv Med Oncol. 2012;4:255–70.
76. Antonescu CR, DeMatteo RP. CCR 20th anniversary commentary: a genetic mechanism of Imatinib resistance in gastrointestinal stromal tumor—where are we a decade later? Clin Cancer Res. 2015;21:3363–5.
77. Catalano F, Cremante M, Dalmasso B, Pirrone C, Lagodin D'Amato A, Grassi M, et al. Molecular tailored therapeutic options for advanced gastrointestinal stromal tumors (GISTs): current practice and future perspectives. Cancers. 2023;15:2074.
78. Zalcberg JR. Ripretinib for the treatment of advanced gastrointestinal stromal tumor. Ther Adv Gastroenterol. 2021;14:17562848211008177.
79. Liu X, Yu J, Li Y, Shi H, Jiao X, Liu X, Guo D, Li Z, Tian Y, Dai FJCD. Disease: Deciphering the tumor immune microenvironment of imatinib-resistance in advanced Gastrointestinal stromal tumors at single-cell resolution. Cell Death Dis. 2024, 15:190.

Publisher's note